

---

---

# Nonconventional 3D Imaging Using Wavelength-Dependent Speckle

Lyle G. Shirley and Gregory R. Hallerman

■ We describe a technique known as speckle-pattern sampling for noncontact measurement of an object's surface contour. In this technique, the object is flood illuminated by a tunable laser, and the wavelength and spatial dependence of the resulting speckle pattern in the scattered light are Fourier analyzed to yield a 3D image of the scattering surface. The theoretical analysis includes a treatment of image aberrations and near-field effects. The technique is demonstrated with laboratory measurements that show good agreement with results from standard contact-based measurements. Range resolutions of better than  $10\ \mu\text{m}$  are achieved. This technique has two principal advantages over many other noncontact methods: the range resolution does not degrade as the distance to the object increases, and the source and receiver lie in the same direction so that the image is not affected by shadowing.

**T**HIS ARTICLE DESCRIBES a nonconventional 3D imaging technique based on the wavelength dependence of laser speckle. The technology grew out of work reported in an earlier article in this journal on applications of laser speckle to target discrimination in ballistic missile defense [1]. Since that time, additional work in the area of 3D imaging has been motivated by applications in advanced manufacturing and dimensional metrology.

In the 3D-imaging technique described here, the object is flood illuminated by a laser beam and the radiation pattern is sampled by a detector array. Because the illumination beam is coherent and the surface of the scattering object has roughness on the scale of a wavelength of light, phase irregularities occur in the scattered light coming from different scattering regions on the surface. Interference among the various contributions to the optical field produces a speckle pattern of bright and dark regions of intensity in the radiation pattern. As the laser is scanned in frequency, this speckle pattern appears to boil, and

changes from the original pattern. We investigate theoretically and experimentally how this speckle pattern is related to the scattering object and describe a technique for forming a 3D image of the scattering surface based on Fourier analysis of the wavelength-dependent speckle intensity. Atmospheric turbulence effects are not treated.

Two features that distinguish the approach taken here from the approach in the earlier article in this journal are that the current work is nonstatistical in nature and that a 3D image of the surface of the object is produced. In the earlier statistical approach, measurements of the wavelength dependence of speckle were taken at multiple positions in space to average out variations due to speckle in the estimate of the object's range-resolved laser radar cross section. Although the range-resolved laser radar cross section is rich in information about the scattering object's size and shape, it falls short of providing a full 3D image of the surface of the object. In the current article, 3D images are produced by combining the

range information obtained by tuning the laser and the cross-range information available from the location in space of individual speckle measurements. Because the current approach is nonstatistical, the mathematical analysis is more straightforward. Consequently, it is not necessary to read the theoretical treatment in Reference 1 to understand the following material on 3D imaging.

Researchers have recognized for many years that the wavelength dependence of scattered electromagnetic radiation carries information about the physical properties of the scattering object. Crystallographers realized early on that the 3D Fourier-transform space of a crystal lattice can be accessed through X-ray diffraction [2]. For a given direction of incidence and a given wavelength, the region of Fourier space being accessed lies on the surface of a sphere known as the Ewald sphere of reflection (see the sidebar entitled “The Ewald Sphere”) [3–5]. E. Wolf appears to have been the first to recognize the connection between the Ewald sphere and optical scattering, and he proposed the use of holographic data to determine 3D

structure [6, 7]. This concept of sampling Fourier space is now a well-known technique in the field of inverse scattering [5–11].

With the advent of tunable lasers, the wavelength dependence of speckle became readily observable. N. George et al. carried out pioneering investigations that related the wavelength-dependent speckle to the scattering object [12–17]. More recently, various imaging techniques based on the wavelength dependence of laser speckle and on tunable laser radars have been proposed and demonstrated [18–39]. The technique presented here, referred to as speckle-pattern sampling (SPS), is based on the concept of sampling the 3D Fourier space of the scattering object. This technique is most similar to one described by J.C. Marron et al. [33, 34].

### Theory

We now develop the mathematical framework for the speckle-pattern-sampling technique. Figure 1 shows the basic measurement procedure to be analyzed. The object is flood illuminated by a tunable laser and the

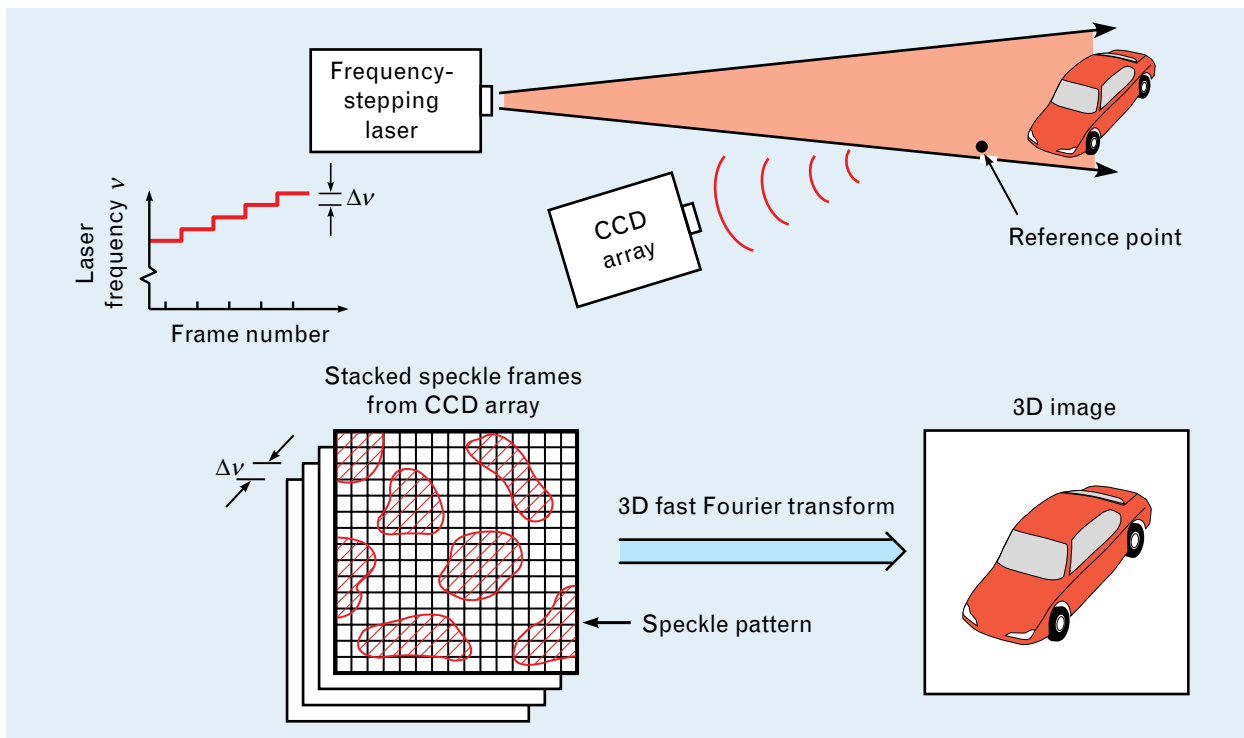


**FIGURE 1.** 3D imaging concept based on speckle-pattern sampling. A tunable laser flood-illuminates the object, and the speckle pattern in the scattered light is sampled at a series of laser frequencies. The resulting speckle frames are stacked to form a 3D array and Fourier transformed to produce a 3D image of the scattering object.

## THE EWALD SPHERE

THE EWALD-SPHERE representation is a geometrical construction for visualizing the region of 3D Fourier space accessible through scattering measurements [2–5]. Figure A shows the two types of spheres to be considered. The first—the Ewald sphere of reflection—has a radius of  $1/\lambda$  in 3D Fourier space with one point of the surface of the sphere attached to the origin of Fourier space and the center of the sphere offset away from the direction of illumination. The surface of the Ewald sphere of reflection defines the region of Fourier space accessible for a particular wavelength and illumination direction. Each point on the surface of this sphere corresponds to a different observation direction for detecting the scattered radiation.

The second type of sphere—the limiting sphere—has a radius of  $2/\lambda$  centered at the origin of Fourier space. The interior of this sphere represents the volume of Fourier space that could be accessed by keeping the wavelength fixed and combining the Ewald spheres of reflection for all possible illumination directions. A reconstructed 3D image is obtained by sampling Fourier space and performing an inverse 3D Fourier transform. The larger the volume of Fourier space sampled, the better the resolution achievable. Resolution cell sizes as small

as  $\lambda/2$  in each dimension can be achieved by sampling the entire volume within the limiting sphere. Sampling of even a small fraction of this volume can yield micron-level resolutions.

There are several approaches to sampling Fourier space, depending on which of the three parameters—wavelength, illumination direction, and observation direction—are varied in a measurement. In the applications we consider in this article, the illumination direction is fixed and Fourier space is sampled by changing the radius of the Ewald sphere of reflection through control of the laser wavelength  $\lambda$ . Thus the sampled region of Fourier space is bounded by the Ewald spheres of

reflection for the minimum and maximum wavelengths used in the measurement. For a near-monostatic measurement configuration (in which the receiver locations and source position are in close proximity), the sampled region of the Ewald sphere of reflection corresponds to the area of the sphere farthest away from the origin of Fourier space, as shown in Figure A. Consequently, there is an offset of  $2/\lambda$  in sampling Fourier space. This offset has a minimal effect on image quality for objects with diffusely scattering surfaces because the surface roughness tends to scatter light in all directions so that information about the underlying shape is distributed in Fourier space.

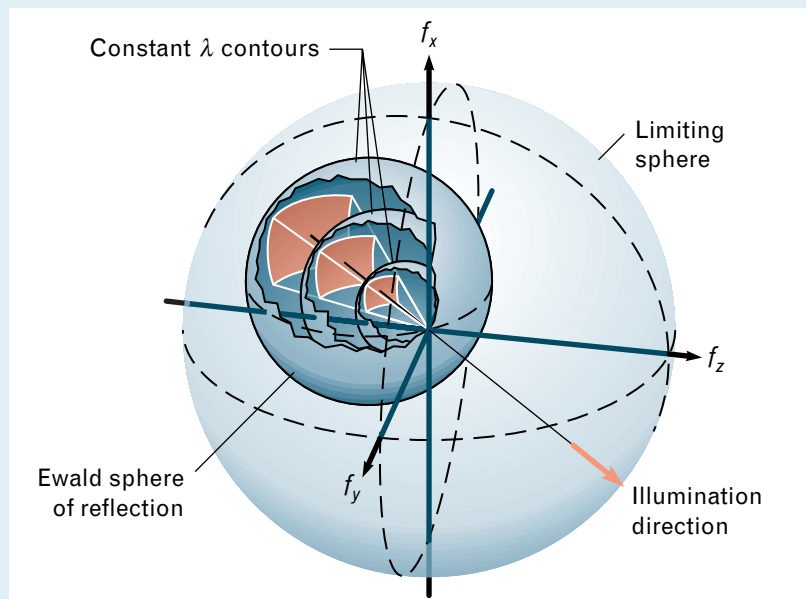


**FIGURE A.** Ewald-sphere representation of the region of Fourier space accessible through scattering measurements.

resulting speckle pattern is measured with a detector array at equally spaced laser frequencies. Individual speckle frames corresponding to successive frequencies are stacked to form a 3D data array. The 3D Fourier transform of this array is then calculated, producing another 3D array representing the 3D autocorrelation function of the 3D image of the object. The reflective reference point located near the scattering object causes bright voxels (volume elements) to appear in certain regions of the 3D array that represent the location in space of scattering cells on the surface of the object. The 3D image is formed by recording the location of these bright voxels.

The preceding description of a speckle-pattern-sampling measurement applies to low-resolution and moderate-resolution 3D imaging. As the frequency-scan length of the laser increases and the solid angle subtended by the detector array increases, the resolution of the 3D image also increases, causing a mixing of the wavelength dependence and the spatial dependence of the speckle pattern. More sophisticated data acquisition or signal processing is then required (see the sidebars entitled “Speckle Size and Shape” for a description of the spatial properties of speckle, and “Wavelength Dependence of Speckle” for an overview of how wavelength dependence is modeled). The following treatment of the speckle-pattern-sampling technique covers these high-resolution effects and summarizes near-field effects caused by noncollimated illumination and detector arrays located in the near field of the object. Additional detail can be found in Reference 39.

### Scattering Model

The first step in analyzing speckle-pattern sampling is to formulate a scattering model that adequately predicts the wavelength dependence of speckle intensity at a given point in the radiation pattern. Figure 2 illustrates the coordinate system for this analysis. Here  $P_s$  represents a monochromatic point source of wavelength  $\lambda$  located at coordinates  $(x_s, y_s, z_s)$  and  $P_r$  represents a reflective reference point located near the object at coordinates  $(x_r, y_r, z_r)$ . To write an expression for the speckle intensity at the observation point  $P_d$  located at  $(x_d, y_d, z_d)$ , we must first calculate the resultant complex amplitude  $V$  of the optical field at

$P_d$  due to scattering from the object’s surface  $b$ . We do this by first considering the contribution from an individual scattering point  $P_b$  located at position  $(x_b, y_b, z_b)$  on the surface. Let us assume that single scattering dominates so that light travels from  $P_s$  to  $P_b$  to  $P_d$  without being scattered from  $P_b$  to other points on the surface before reaching  $P_d$ . The phase delay at  $P_d$  due to this propagation path length is obtained by adding the distance  $R_{sb}$  from  $P_s$  to  $P_b$  and the distance  $R_{bd}$  from  $P_b$  to  $P_d$  and multiplying the sum by the wave number  $k = 2\pi/\lambda$ . The resulting contribution to the complex amplitude at  $P_d$  is

$$V_b(x_d, y_d, z_d; \lambda) = g(x_b, y_b, z_b) \exp\left[-i \frac{2\pi}{\lambda} (R_{sb} + R_{bd})\right]. \quad (1)$$

In Equation 1,  $g(x_b, y_b, z_b)$  is a complex scattering function whose magnitude represents the strength of the contribution from  $P_b$  and whose phase accounts for any phase change caused by scattering. The complex amplitude resulting from the entire surface is obtained by summing the individual contributions from all scattering points. Because the scattering function is zero valued at locations where there are no scattering points, this summation can be written as an integral over all space:

$$V(x_d, y_d, z_d; \lambda) = \int_{-\infty}^{\infty} \int_{-\infty}^{\infty} \int_{-\infty}^{\infty} g(x_b, y_b, z_b) \times \exp\left[-i \frac{2\pi}{\lambda} (R_{sb} + R_{bd})\right] dx_b dy_b dz_b. \quad (2)$$

The distances  $R_{sb}$  and  $R_{bd}$  in Equation 2 are given by

$$R_{sb} = \sqrt{(x_s - x_b)^2 + (y_s - y_b)^2 + (z_s - z_b)^2} \quad (3)$$

and

$$R_{bd} = \sqrt{(x_b - x_d)^2 + (y_b - y_d)^2 + (z_b - z_d)^2}. \quad (4)$$

If the height profile of the scatterer is represented by  $h(x, y)$ , then we can write the scattering function as

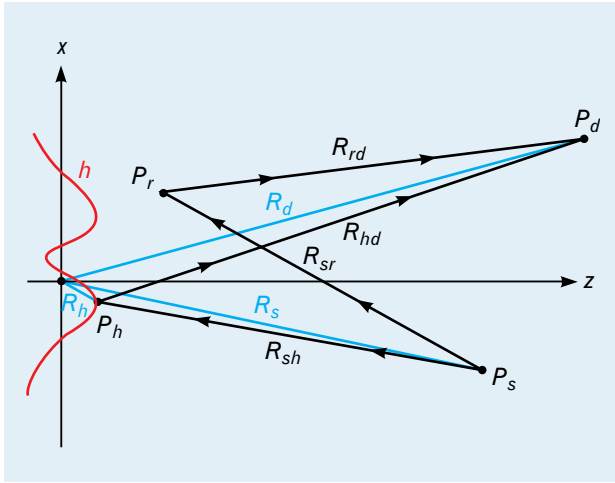


**FIGURE 2.** The coordinate system for the analysis of 3D imaging, showing the source point  $P_s$ , scattering point  $P_h$ , reference point  $P_r$ , and observation point  $P_d$ .

$$g(x, y, z) = a(x, y) \delta[z - h(x, y)], \quad (5)$$

where  $a(x, y)$  is the complex amplitude of the given contribution to  $V$ . Our primary objective in 3D imaging is to recover the functional form of  $h(x, y)$ ; the recovery of  $a(x, y)$  is a more difficult problem that is of less interest, and is not considered here.

The total complex amplitude at the observation point  $P_d$  is the sum of contributions from the surface, as given by Equation 2, and the contribution  $V_r$  from the reference point. If  $g_r$  is a complex amplitude representing the strength of the reference point and any phase shift associated with it, then this contribution from the reference point can be written in a manner similar to Equation 1 as

$$V_r(x_d, y_d, z_d; \lambda) = g_r \exp\left[-i \frac{2\pi}{\lambda} (R_{sr} + R_{rd})\right]. \quad (6)$$

The distances  $R_{sr}$  and  $R_{rd}$  in Equation 6 are given by Equations 3 and 4, respectively, with the subscript  $h$  replaced by the subscript  $r$  in each case. Finally, the quantity measured at the observation point is the magnitude squared of the total complex amplitude:

$$\begin{aligned} I(x_d, y_d, z_d; \lambda) &= |V_r + V|^2 \\ &= I_1 + I_2 + I_3 + I_4. \end{aligned} \quad (7)$$

The individual intensity terms in Equation 7 are

$$I_1 = |g_r|^2, \quad (8)$$

$$I_2 = |V(x_d, y_d, z_d; \lambda)|^2, \quad (9)$$

$$\begin{aligned} I_3 &= g_r^* \exp\left[-i \frac{2\pi}{\lambda} (R_{sr} + R_{rd})\right] \\ &\quad \times V(x_d, y_d, z_d; \lambda), \end{aligned} \quad (10)$$

and

$$I_4 = I_3^*. \quad (11)$$

Equation 7 and the corresponding expressions for the four terms  $I_1$  through  $I_4$  in Equations 8–11 serve as our model for describing the spatial and wavelength dependence of laser speckle.

### 3D-Image Formation

We now explore the meaning of the four intensity terms in Equation 7 and show how they relate to the desired 3D image of the scattering object. To facilitate this analysis, we must approximate the distances  $R_{sh}$  and  $R_{hd}$  defined by Equations 3 and 4. The basis for approximating these quantities is the assumption that the distance  $R_b$  between the origin and a scattering point on the surface in Figure 2 is small compared with  $R_s$  and  $R_d$  (which are defined as the distances from the origin to the points  $P_s$  and  $P_d$ , respectively). The most basic approximation is the far-field, or Fraunhofer, approximation, which retains only those terms in a series expansion of  $R_{sh}$  or  $R_{hd}$  (in terms of  $R_b$ ) that are linear in  $R_b$ . This approximation restricts the object size for practical observation distances. Larger objects can be handled by using the Fresnel approximation, which retains terms up to second order in  $R_b$ .

We consider both the far-field and Fresnel approximations in this article. Although the far-field approximation may limit the object size, it does provide the framework for introducing the basic principles of 3D imaging. Consequently, most of the following results are based on this approximation. (Size restrictions inherent in the far-field approximation can be overcome in practice by illuminating the ob-

## SPECKLE SIZE AND SHAPE

BECAUSE THE 3D imaging technique described in the main text is based on observing variations of speckle intensity in the radiation pattern of a scattering object, it is beneficial to summarize the basic size and shape dependence of speckle. First, we need to know the transverse speckle size along the detector plane to ensure that the detector elements are small enough to sample individual speckle lobes. Second, we must understand how quickly the speckle pattern varies longitudinally with changes of distance from the scatterer.

Figure A illustrates how the average transverse and longitudinal size of a speckle lobe grow with distance. In this figure,  $d_{\perp}$  is the average transverse speckle size that would be observed on the interior surface of a sphere of radius  $R$  centered around the scattering object. If  $D$  represents the projected linear size extent of the illuminated portion of the scattering object for a given observation angle, then the average speckle size  $d_{\perp}$  in the direction along which  $D$  is measured is

$$d_{\perp} = \lambda \frac{R}{D}. \quad (\text{A})$$

Equation A shows that speckle size is proportional to the wavelength  $\lambda$  and the range  $R$  but inversely proportional to the size  $D$ .

In Figure A, the average longi-

tudinal speckle size that would be observed in the radial direction at the distance  $R$  is denoted by  $d_{\parallel}$ . An expression for  $d_{\parallel}$  in the Fresnel zone is given in the literature (see References 17 and 40) as

$$d_{\parallel} = 4\lambda \frac{R^2}{D^2}. \quad (\text{B})$$

Thus the longitudinal speckle size grows as the square of the distance  $R$  rather than linearly with  $R$ , so there is a rapid elongation of the speckle lobes with distance. Once the observation point is in the far field, the intensity of the speckle pattern does not change in the radial direction, except for falling off as  $1/R^2$ .

In a typical laboratory setup, with  $D = 50$  mm,  $R = 2$  m, and  $\lambda = 0.8$   $\mu\text{m}$ , the average transverse speckle size at the receiver plane is  $d_{\perp} = 32$   $\mu\text{m}$ , which matches well with the pixel size of a typical CCD detector. Since this range is not yet in the far field, the speckle intensity is still fluctuating in the radial direction. The longitudinal speckle size, from Equation B, is

$d_{\parallel} = 5.1$  mm. This relatively slow variation of the speckle pattern with  $R$  may allow the methods described in the main text to be applied to objects with longitudinal motion components.

To illustrate further the spatial properties of speckle, we show a 3D measured speckle pattern in Figure B. This pattern was obtained by back-illuminating a ground-glass diffuser with a focused laser beam from a HeNe laser and sampling the resulting speckle pattern with a CCD array. The CCD array was translated in the longitudinal direction between frames and the frames were combined into a 3D array representing the speckle intensity as a function of position. The conical region containing the speckle pattern is 300  $\mu\text{m}$  in length and its diameter increases from 25  $\mu\text{m}$  to 100  $\mu\text{m}$ . In acquiring the data, we had to use a microscope objective to magnify the speckle and to image the plane of interest onto the CCD array. The intensity was normal-

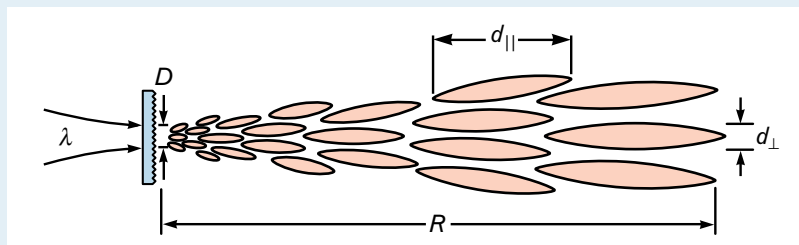


**FIGURE A.** Average transverse and longitudinal speckle size. The speckle lobes elongate with increasing distance from the scattering surface.

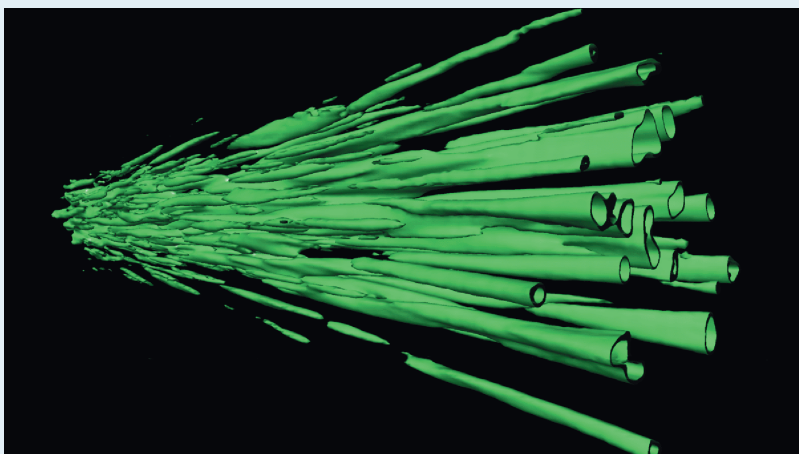


**FIGURE B.** Measured 3D speckle pattern from a ground-glass diffuser back illuminated by a 25- $\mu\text{m}$ -diameter 0.633- $\mu\text{m}$ -wavelength HeNe laser spot. The image was formed by stacking a series of 150 CCD images of the speckle pattern, with a longitudinal displacement of 2  $\mu\text{m}$  between frames.

ized (by dividing by  $R^2$ ) and rendered as an isosurface to visualize the speckle pattern more easily in three dimensions.

Figure C shows the relation between speckle shape and transverse object shape for three different objects. For the triconic, the

individual speckle lobes are elongated in the direction perpendicular to the axis of the triconic. For the sphere, the speckle lobes appear to wrap around one another like worms in a bucket. No direction is preferred, and the speckle shape is symmetric on average. For the ring, the borders of the individual speckle lobes appear to be better defined. From these measurements, the transverse structure of the speckle pattern clearly not only provides a measure of the size of the object but also carries information about its orientation and transverse shape. The main text of the article describes how to extract this information by using Fourier analysis.

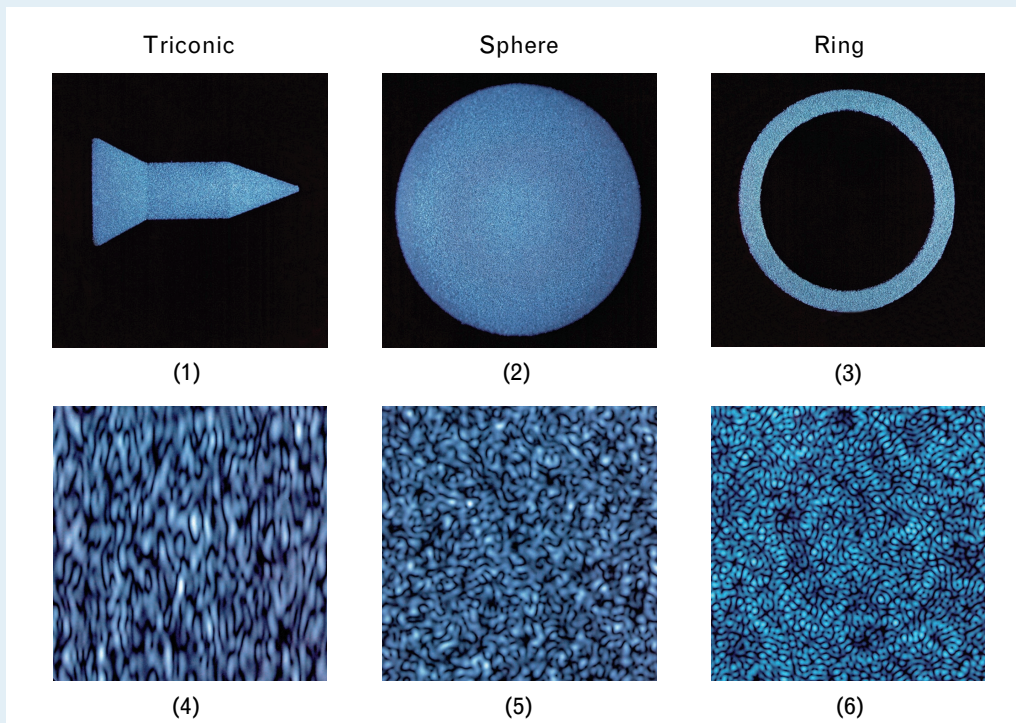


**FIGURE C.** Effect of object shape on speckle patterns. Three different geometric objects were laser illuminated: (1) a 25-mm-long triconic, (2) a 25-mm-diameter sphere, and (3) a ring with an outer diameter of 25 mm and an inner diameter of 20 mm. The corresponding speckle patterns are shown in (4), (5), and (6), respectively.

## WAVELENGTH DEPENDENCE OF SPECKLE

WHEN AN OBJECT is illuminated by a tunable laser, the speckle pattern present in the scattered light changes as the laser frequency varies. This sidebar explains why this variation occurs, and shows how the rate at which it occurs is related to the range extent of the object.

We use Figure A to develop a basic understanding of the wavelength dependence of speckle. In Figure A(1), a seven-level step target is flood illuminated with a collimated laser beam propagating along the positive  $z$ -axis. The frequency dependence of the speckle intensity at a distant point  $P$  lying on the negative  $z$ -axis can be determined by adding the complex amplitude of the optical field of the contributions from each of the seven levels. These contributions are represented by the phasors (in blue) located below each level (a harmonic time dependence is suppressed). The magnitude of these phasors represents the strength of the return, and the orientation represents the relative phase of each contribution. The relative phase is a combination of the phase due to wave propagation between scattering planes and a random component that accounts for the surface roughness. Figure A(2) shows the resultant phasor obtained by placing the components end to end in the

complex plane (blue lines). The optical intensity, or irradiance, is proportional to the magnitude squared of the resultant, shown by the blue dot in Figure A(3). The phase of the resultant is given by the blue dot in Figure A(4).

Now consider the effect that changing the laser frequency  $\nu$  has on the resultant complex amplitude at point  $P$ . Let  $\phi$  represent the component of the phase for a given height level that arises from wave propagation. If  $\phi$  is measured with respect to the  $z = 0$  plane (defined by the first height level on the left), the phase delay for propagation from this plane to a plane with range  $z$  is

$$\phi = 2\pi \frac{z}{\lambda} = 2\pi \frac{z\nu}{c},$$

where  $\lambda$  is the wavelength and  $c$  is the speed of light. Therefore, at a given range  $z$ , a change in frequency of  $\Delta\nu$  introduces a phase shift, or phasor rotation, of

$$\Delta\phi = 2\pi \frac{2z}{c} \Delta\nu \quad (\text{A})$$

for round-trip propagation between the two planes. Equation A can now be used to determine how much a given frequency change  $\Delta\nu$  rotates each phasor in Figure A(1). The red phasors correspond to a frequency shift of  $\Delta\nu = c/(8L)$ , which is the frequency shift required to rotate the phasor at the  $z = L$  plane by

$\Delta\phi = 90^\circ$ . Because of the linear relation between phase shift and distance, the phasor at the  $L/2$  plane is rotated by  $45^\circ$  and the phasor at the  $L = 0$  plane is stationary. The red dot in Figure A(2) shows the new resultant. Because the magnitude increases, so does the intensity in Figure A(3). The phase in Figure A(4) also increases because the resultant in Figure A(2) happens to rotate in the counterclockwise direction. Observe that a phasor rotation of  $90^\circ$  at the  $z = L$  plane is insufficient to decorrelate the speckle intensity. The curved path in Figure A(2) represents the trajectory that the resultant complex amplitude takes as the frequency varies. As illustrated by the green dots in Figures A(2)–A(4), a rotation of  $360^\circ$  is adequate for decorrelation. For this value, the phasor at  $z = L/2$  is  $180^\circ$  out of phase (even though the phasor at  $z = L$  is back in phase), producing a different resultant. If a  $360^\circ$  rotation is used as the basis for defining the decorrelation frequency  $\Delta\nu_D$ , then

$$\Delta\nu_D = \frac{c}{2L}. \quad (\text{B})$$

As an illustration of Equation B, the decorrelation frequency for an object with a range extent of 100 mm is 1.5 GHz.

As the length of the laser-frequency scan increases beyond the

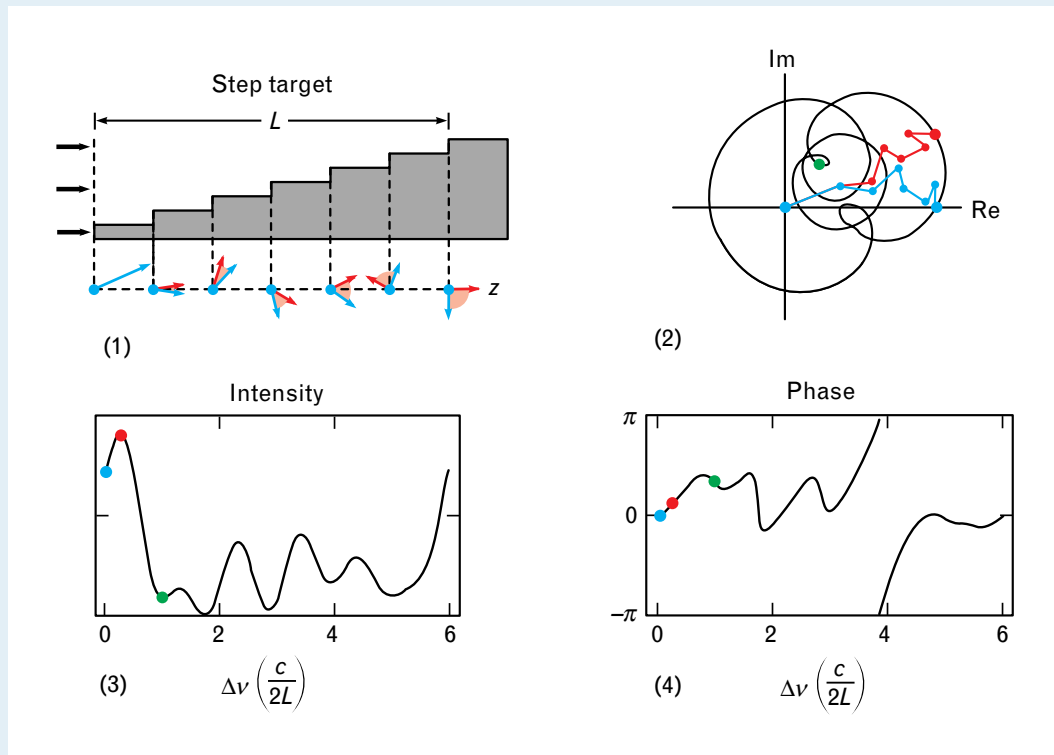


**FIGURE A.** Frequency dependence of the on-axis speckle intensity from a step target: (1) step target with phasors indicating contributions from each step for two frequencies; (2) path of resultant complex amplitude in the complex plane; (3) frequency dependence of intensity; (4) frequency dependence of phase.

value of the decorrelation frequency  $\Delta\nu_D$ , more and more oscillations occur in the speckle intensity. As the number of oscillations increases, so does our ability to resolve the object in range. It turns out that the number of raw range-resolution cells along the range extent  $L$  of the object is equal to the number of speckle oscillations. In terms of the tuning range  $B$ , the raw range resolution  $\Delta z$  is given (see Equation 41 in the main text) by

$$\Delta z = \frac{c}{2B}. \quad (\text{C})$$

As an example of Equation C, a range resolution of 1 mm can be

achieved by scanning the laser over a bandwidth of 150 GHz—a small frequency excursion for a typical tunable laser.

Another important observation about the wavelength dependence of speckle is that the fluctuating speckle intensity produced by scanning the laser frequency is band limited, or has a highest frequency of oscillation, so that the speckle intensity cannot change any faster than this highest-frequency component. Because large oscillation frequencies correspond to large range offsets between scattering cells, the cutoff frequency that band-limits the speckle-intensity sequence is just

the decorrelation frequency  $\Delta\nu_D$  corresponding to the total range extent  $L$  in Equation B. By the Nyquist sampling theorem, we must sample the speckle-intensity sequence at least twice during each of these highest-frequency oscillations. This sampling condition leads to the conclusion that the laser-frequency step size between samples must obey the expression

$$\Delta\nu_{\text{step}} \leq \frac{c}{4L}. \quad (\text{D})$$

For example, an object with a range extent of 100 mm would require a laser-frequency step size of 750 MHz or less.

ject with collimated light and placing a Fourier-transform lens in front of the detector array to simulate far-field observation.) The section on near-field effects is based on the Fresnel approximation. This section shows that good images can be obtained much farther into the near field than would be expected on the basis of the validity conditions for the far-field approximation.

Let us consider the distance  $R_{hd}$ . Its far-field approximation is given by

$$R_{hd} \approx R_d - \frac{x_h x_d + y_h y_d + z_h z_d}{R_d}. \quad (12)$$

(A similar expression holds for  $R_{sb}$ , with the subscript  $d$  replaced by the subscript  $s$ .) A validity condition

for Equation 12, obtained by requiring that second-order terms in  $R_b$  introduce phase errors of less than  $\pi/2$  for any direction of observation and any offset direction of  $R_b$  from the origin, is given by

$$R_d > \frac{2R_b^2}{\lambda}. \quad (13)$$

Rather large observation distances are required to satisfy Equation 13. For example, an observation distance  $R_d$  of at least 250 m is necessary for an object size  $R_b$  of 10 mm and a wavelength  $\lambda$  of  $0.8 \mu\text{m}$ . The corresponding validity condition for the Fresnel approximation is

$$R_d^3 > \frac{R_b^4}{2\lambda}. \quad (14)$$

This approximation is valid for the same object at an observation distance  $R_d$  of only 185 mm.

For now, we continue the analysis using the far-field approximation. To find the speckle intensity, we must first evaluate Equation 2 for the complex amplitude  $V$ . Substitution of the approximation for  $R_{hd}$  given in Equation 12 and the corresponding expression for  $R_{sb}$  into Equation 2 yields

$$\begin{aligned} V(x_d, y_d, z_d; \lambda) &= \exp\left[-i\frac{2\pi}{\lambda}(R_s + R_d)\right] \int_{-\infty}^{\infty} \int_{-\infty}^{\infty} \int_{-\infty}^{\infty} g(x_b, y_b, z_b) \\ &\times \exp\left\{-i\frac{2\pi}{\lambda}\left[x_b\left(\frac{x_s}{R_s} + \frac{x_d}{R_d}\right) + y_b\left(\frac{y_s}{R_s} + \frac{y_d}{R_d}\right) + z_b\left(\frac{z_s}{R_s} + \frac{z_d}{R_d}\right)\right]\right\} dx_b dy_b dz_b. \end{aligned} \quad (15)$$

Note that the integral in Equation 15 is the 3D Fourier transform of  $g(x, y, z)$ , defined as

$$\begin{aligned} \bar{g}(f_x, f_y, f_z) &= \int_{-\infty}^{\infty} \int_{-\infty}^{\infty} \int_{-\infty}^{\infty} g(x, y, z) \\ &\times \exp[-i2\pi(f_x x + f_y y + f_z z)] dx dy dz, \end{aligned}$$

which allows us to rewrite Equation 15 as

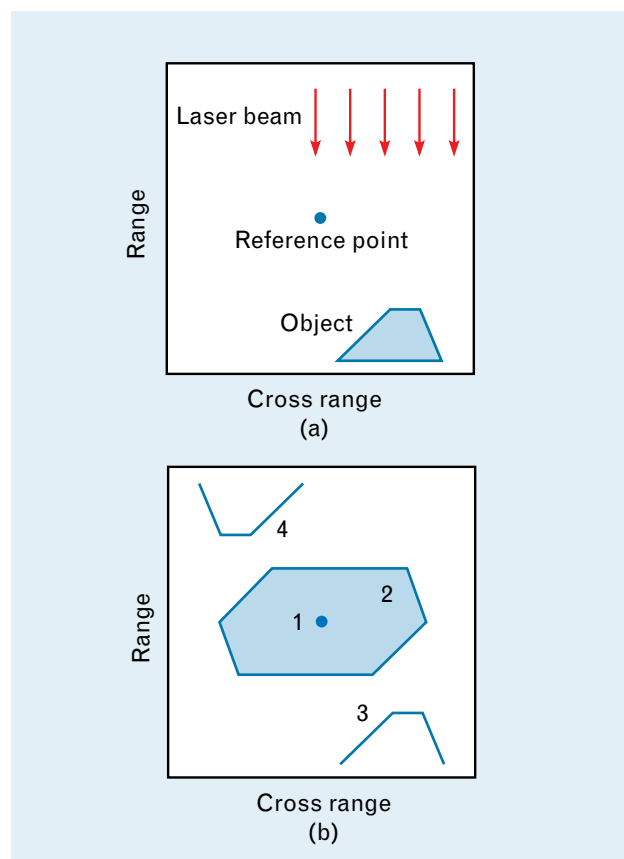


**FIGURE 3.** Interpretation of the 3D Fourier transform of a speckle-pattern-sampling data set: (a) object scene; (b) components in image space representing the 3D Fourier transform of the four terms in Equation 24. These components are (1) a 3D delta function, (2) a 3D autocorrelation function of the scattering function, (3) the desired image, and (4) the inverted image.

$$V(x_d, y_d, z_d; \lambda) = \exp\left[-i \frac{2\pi}{\lambda} (R_s + R_d)\right] \bar{g}(f_x, f_y, f_z). \quad (16)$$

In Equation 16, the spatial frequencies  $f_x$ ,  $f_y$ , and  $f_z$  are given by

$$f_x = -\frac{l_s + l_d}{\lambda}, \quad (17)$$

$$f_y = -\frac{m_s + m_d}{\lambda}, \quad (18)$$

and

$$f_z = -\frac{n_s + n_d}{\lambda}, \quad (19)$$

where  $l_s = x_s/R_s$ ,  $m_s = y_s/R_s$ , and  $n_s = z_s/R_s$  are direction cosines corresponding to the source point  $(x_s, y_s, z_s)$ ; and  $l_d = x_d/R_d$ ,  $m_d = y_d/R_d$ , and  $n_d = z_d/R_d$  are direction cosines corresponding to the observation point  $(x_d, y_d, z_d)$ . Note that any two of the three direction cosines determine the third direction cosine (to within a sign) through the relations

$$l_s^2 + m_s^2 + n_s^2 = 1 \quad (20)$$

and

$$l_d^2 + m_d^2 + n_d^2 = 1. \quad (21)$$

Now that the Fourier-transform relation has been established and the spatial frequencies have been defined, we can substitute Equation 16 into Equations 9 and 10 to obtain

$$I_2 = \left| \bar{g}(f_x, f_y, f_z) \right|^2 \quad (22)$$

and

$$I_3 = g_r^* \bar{g}(f_x, f_y, f_z). \quad (23)$$

(In writing Equation 23, we have assumed, without loss of generality, that the reference point  $P_r$  is located at the origin so that  $R_{sr}$  and  $R_{rd}$  can be replaced by  $R_s$  and  $R_d$  in Equation 6 for the reference term.) Equation 7 now takes the form

$$I(x_d, y_d, z_d; \lambda) = |g_r|^2 + \left| \bar{g}(f_x, f_y, f_z) \right|^2 + g_r^* \bar{g}(f_x, f_y, f_z) + g_r \bar{g}^*(f_x, f_y, f_z). \quad (24)$$

The significance of the four terms  $I_1$  through  $I_4$  in Equation 24 becomes evident by performing an inverse 3D Fourier transform to convert from Fourier space to object space. Figure 3 illustrates the inverse Fourier transforms of the individual terms. The scattering surface, shown in Figure 3(a), is located below and to the right of the reference point. Because  $I_1$  is a constant, its inverse Fourier transform is a 3D  $\delta$ -function located at the origin of object space in Figure 3(b). By the autocorrelation theorem, the inverse Fourier transform of  $I_2$  is the 3D autocorrelation function of  $g(x, y, z)$ . The support of this autocorrelation function is shown in the region surrounding the origin in Figure 3(b). Note that the  $I_2$  term occurs with or without the use of a reference point (see the sidebar entitled "Remote Orientation Sensing" for a description of a technique for remote orientation sensing that utilizes this term).

The inverse 3D Fourier transform of  $I_3$  yields the scattering function  $g(x, y, z)$ , multiplied by the complex conjugate of the strength of the reference point:

$$\begin{aligned} & \int \int \int_{-\infty}^{\infty} I_3(f_x, f_y, f_z) \\ & \times \exp[i2\pi(f_x x + f_y y + f_z z)] df_x df_y df_z \\ & = g_r^* g(x, y, z). \end{aligned}$$

This term corresponds to the desired image and occurs in the lower right quadrant of Figure 3(b). By Equation 5,  $g(x, y, z)$  is localized in space to the surface of the scattering object. Thus bright regions in the magnitude of the Fourier transform of  $I_3$  occur at values of  $x$ ,  $y$ , and  $z$  such that

$$z = h(x, y), \quad (25)$$

defining the surface profile, or 3D image, of the scattering object. Because  $I_4$  is the complex conjugate of  $I_3$ , its inverse Fourier transform is  $g_r^* g(-x, -y, -z)$ . This term corresponds to the inverted image shown

## REMOTE ORIENTATION SENSING

FOR MANY APPLICATIONS in robotics and machine vision, it is desirable to remotely measure the orientation of an object or a surface of an object. This sidebar describes a technique based on the wavelength dependence of laser speckle for accomplishing this task. The technique can be implemented with a minimal system and does not require a reference point or multiple frames of data. Its basis is the fact that, for a flat surface, a change in laser frequency produces a global translation of the speckle pattern at the detector plane. Knowledge of the direction and rate of speckle shift allows us to determine the normal vector to the surface.

Figure A illustrates the measurement geometry. The beam propagates along the negative  $z$  direction. We wish to determine the angle of incidence  $\theta_b$  and the azimuthal angle  $\phi_b$  of the normal vector to the surface. We proceed by writing the height profile  $h(x, y)$  of a tilted flat plate as

$$h(x, y) = h_0 - x \cos \phi_b \tan \theta_b - y \sin \phi_b \tan \theta_b, \quad (\text{A})$$

where  $h_0$  is the height of the plate at  $x = y = 0$ . Equation 5, which is repeated here for convenience,

$$g(x, y, z) = a(x, y) \delta[z - h(x, y)], \quad (\text{B})$$

can now be used to express the scattering function  $g(x, y, z)$  for the tilted plate in terms of its complex amplitude  $a(x, y)$  and a  $\delta$ -function limiting the scattering function to the planar surface.

To predict the effect that tuning the laser frequency has on the speckle pattern, we first note that the speckle intensity at a point in the far field of a scattering object is essentially the magnitude squared of the Fourier transform of the object's scattering function, as given by Equation 22:

$$I(x_d, y_d, z_d; \lambda) = |\tilde{g}(f_x, f_y, f_z)|^2. \quad (\text{C})$$

In Equation C, the tilde represents a Fourier transform, and  $f_x$ ,  $f_y$ , and  $f_z$  are spatial-frequency variables. For observation points

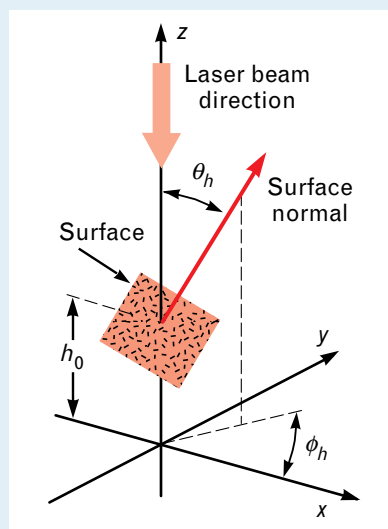


**FIGURE A.** Coordinate system for surface-orientation measurement.

near the  $z$ -axis and for small variations  $\Delta\nu$  in laser frequency, the spatial-frequency variables take the form

$$f_x = -\frac{x_d}{\lambda_0 z_d}, \quad (\text{D})$$

$$f_y = -\frac{y_d}{\lambda_0 z_d}, \quad (\text{E})$$

and

$$f_z = -2\left(\frac{1}{\lambda_0} + \frac{\Delta\nu}{c}\right), \quad (\text{F})$$

where  $\lambda_0$  is the nominal wavelength (see Equations 29, 30, and 38 in the main text).

We next evaluate the 3D Fourier transform of the scattering function obtained from Equations A and B, and substitute this Fourier transform into Equation C to determine the speckle intensity at the detector plane in terms of spatial-frequency coordinates:

$$|\tilde{g}(f_x, f_y, f_z)|^2 = |\tilde{a}(f_x - f_z \tan \theta_b \cos \phi_b, f_y - f_z \tan \theta_b \sin \phi_b)|^2. \quad (\text{G})$$

We use Equation G to determine the effect that tuning the laser frequency has on individual speckle lobes. Mathematically, we can track the motion of a speckle lobe, as the laser frequency varies, by keeping the arguments of  $\tilde{a}$  constant in Equation G. Thus for the first argument

$$\Delta f_x = \Delta f_z \tan \theta_b \cos \phi_b, \quad (\text{H})$$

and for the second argument

$$\Delta f_y = \Delta f_z \tan \theta_b \sin \phi_b. \quad (\text{I})$$

In Equations H and I,  $\Delta f_x$  and  $\Delta f_y$  are the changes in  $f_x$  and  $f_y$  required, respectively, to track the motion of a speckle lobe, and  $\Delta f_z$  is the corresponding change in  $f_z$  resulting from tuning the laser frequency. Since Equations D through F are linear in  $x_d, y_d$ , and  $\Delta v$ , every speckle lobe in the speckle pattern shifts by the same amount and in the same direction in the detector plane.

The orientation of the scattering surface can be determined by solving Equations H and I for  $\theta_b$  and  $\phi_b$ . In doing so, we can write the spatial-frequency changes in terms of the laser-frequency shift  $\Delta v$  and the magnitude  $\Delta r_d$  and direction  $\phi_d$  of the speckle shift in the detector plane to obtain

$$\tan \theta_b = -\frac{\Delta r_d}{2z_d} \frac{v_0}{\Delta v}, \quad (\text{J})$$

where  $v_0 = c/\lambda_0$ , and

$$\phi_b = \phi_d. \quad (\text{K})$$

Thus the angle of incidence  $\theta_b$  and the plane of incidence  $\phi_b$  can be determined remotely by measuring the magnitude and direction, respectively, of the speckle shift caused by tuning the laser frequency.

To apply Equation J to the determination of  $\theta_b$  in practice, we must know the detector distance  $z_d$ . This requirement can be circumvented, however, by placing a

positive lens one focal length  $f$  in front of the detector array. Then  $z_d$  is replaced by  $f$  in Equation J and the measurement is insensitive to object distance.

To illustrate the technique for remotely sensing surface orientation, we performed laboratory measurements by using the optical system shown in Figure 8. In these measurements, a flat plate was mounted on a system of rotary stages that enabled control of the angle of incidence  $\theta_b$  and the plane of incidence  $\phi_b$ , and the plate was spot illuminated with a beam from a Ti:sapphire laser. The laser frequency was stepped by a known amount and the CCD frames were compared at the two frequencies by calculating a 2D cross correlation of the speckle frames. The magnitude and the direction of offset from the origin of the cross-correlation

peak provided a measurement of  $\Delta r_d$  and  $\phi_d$ . Figure B is a family of plots of the magnitude of the speckle shift (in units of pixels  $\rho$ ) versus laser-frequency shift  $\Delta v$  for angles of incidence  $\theta_b$  ranging between  $10^\circ$  and  $70^\circ$ . In this figure, the  $\rho$  versus  $\Delta v$  curves are straight lines whose slope is proportional to  $\tan \theta_b$ , as predicted by Equation J. We also performed a series of measurements with constant  $\theta_b$  and variable  $\phi_b$  that confirm the linear relation between  $\phi_d$  and  $\phi_b$  predicted by Equation K.

The surface-orientation information available from this technique is valuable in the interpretation of object scenes. It is not necessary for the illuminated surface to be perfectly flat. A by-product of the technique is a means for estimating the flatness from the strength of the cross-correlation peak.

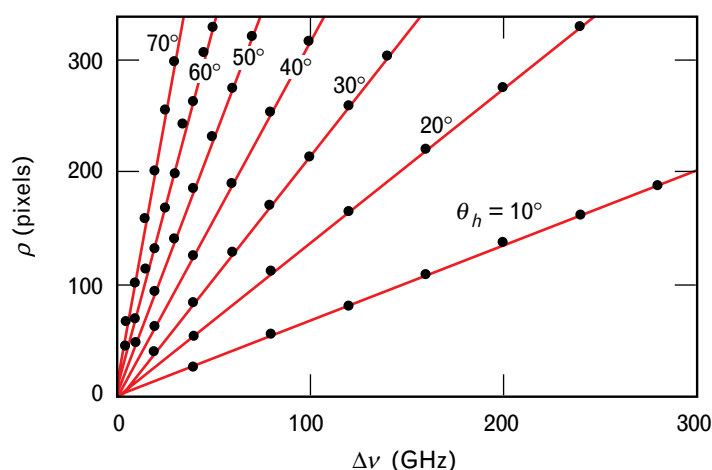


**FIGURE B.** Remote angle-of-incidence measurements for a flat plate illuminated by a tunable laser at various angles. As the laser-frequency offset  $\Delta v$  increases, the speckle pattern shifts from the original position. The magnitude  $\rho$  of the shift increases with angle of incidence.

in the upper left quadrant of Figure 3(b).

Figure 3 indicates that the desired image will be separated from the central autocorrelation function and from the inverted image if the object is far enough away from the reference point. Given that this condition is satisfied, the image can be isolated by selecting the appropriate region of the inverse Fourier transform. It is sufficient for the object to be removed from the reference point by either the object's illuminated range extent or by its cross-range extent in any cross-range direction. Another approach is to use a strong reference point just outside of the object that produces  $I_3$  and  $I_4$  terms that swamp out the autocorrelation term  $I_2$ . Yet another technique for isolating the image term is to incorporate a phase shift  $\phi$  in the reference beam [33] and to measure the speckle pattern by using two different phase-shift values,  $\phi = 0$  and  $\pi$ . By subtracting these two frames for each value of  $\lambda$ , we get the  $I_1$  and  $I_2$  terms to cancel, leaving terms  $I_3$  and  $I_4$ . The advantage of this approach is that the reference point can be located more closely to the object so that Fourier space can be sampled at a lower sampling rate while achieving the same resolution. Still more sparse sampling of Fourier space is possible if the reference point can be located inside the object or can be made to appear so. Then by using the additional phase-shift values of  $\phi = \pi/2$  and  $3\pi/2$ , we can also eliminate the  $I_4$  term.

### Sampling of 3D-Fourier Space

Having shown that we can eliminate the undesired terms in Equation 7, we ignore terms other than  $I_3$  from now on. Our next objective is to develop a strategy for sampling the Fourier space of  $I_3$  at the desired array of spatial frequencies.

According to Equations 17 through 19, different points in Fourier space can be accessed by varying the illumination direction, the observation direction, and the wavelength. The sidebar entitled "Ewald Sphere" gives a geometrical description of the region of 3D Fourier space that can be covered for a given wavelength and a given illumination direction. To find the governing equation for this geometrical construction, we ask ourselves if there is a wavelength  $\lambda$ , for a given illumination direction, that will allow a

given set of spatial frequencies  $f_x$ ,  $f_y$ , and  $f_z$  to be sampled. The required value of  $\lambda$  is obtained by using Equations 20–21 to rearrange Equations 17–19:

$$\lambda = -2 \frac{l_s f_x + m_s f_y + n_s f_z}{f_x^2 + f_y^2 + f_z^2}. \quad (26)$$

For given values of  $l_s$ ,  $m_s$ ,  $n_s$ , and  $\lambda$ , Equation 26 maps out the surface of a sphere of radius  $1/\lambda$  in Fourier space, as described in the Ewald-sphere sidebar.

Given the functional dependence of  $\lambda$  from Equation 26, we can now rewrite Equations 17 and 18 as

$$l_d = -l_s + \lambda f_x \quad (27)$$

and

$$m_d = -m_s + \lambda f_y, \quad (28)$$

and substitute  $\lambda$  from Equation 26 into these equations to express all three measurement variables  $l_d$ ,  $m_d$ , and  $\lambda$  in terms of the desired spatial frequencies  $f_x$ ,  $f_y$ , and  $f_z$ . Thus Equations 26–28 provide a means for determining the wavelength and the direction in space of an observation point required for sampling a particular value of spatial frequency.

In Equations 26–28, the illumination direction either can be fixed or can vary during the sampling of Fourier space. It is fixed in the approach taken in this article. If we place the source on the positive  $z$ -axis, then  $l_s = m_s = 0$  and  $n_s = 1$ , and Equations 17–19 reduce to

$$f_x = -\frac{l_d}{\lambda} = -\frac{x_d}{\lambda R_d}, \quad (29)$$

$$f_y = -\frac{m_d}{\lambda} = -\frac{y_d}{\lambda R_d}, \quad (30)$$

and

$$f_z = -\frac{1 + n_d}{\lambda} = -\frac{1}{\lambda} \left( 1 + \sqrt{1 - \frac{x_d^2 + y_d^2}{R_d^2}} \right).$$

In addition, Equation 26 simplifies to

$$\lambda = -\frac{2f_z}{f_x^2 + f_y^2 + f_z^2}. \quad (31)$$

In principle, the wavelength can be varied according to Equation 31 and the observation point varied according to

$$x_d = -\lambda f_x R_d \quad (32)$$

and

$$y_d = -\lambda f_y R_d \quad (33)$$

(obtained by rearranging Equations 29 and 30) to sample Fourier space at any desired location.

We can gain more insight into the sampling of Fourier space by investigating Equation 31 and its Ewald-sphere representation in greater detail. With the source on the positive  $z$ -axis, the center of the Ewald sphere of reflection for a particular value of  $\lambda$  is located on the  $f_z$ -axis at  $-1/\lambda$ , as illustrated in Figure 4. The surface of the sphere touches the  $f_z$ -axis at the origin and at  $-2/\lambda$ . Let us consider the sampling of Fourier space for small changes in the laser wavelength  $\lambda$  and for small values of  $f_x$  and  $f_y$  (corresponding to those observation points  $x_d$  and  $y_d$  which are close to the  $z$ -axis). If  $\lambda_0$  is the nominal wavelength about which  $\lambda$  is varied, the sampled region of Fourier space lies near the left-most point,  $f_{z_0} = -2/\lambda_0$ , of the Ewald sphere. Thus there is a Fourier-space-sampling offset  $f_{z_0}$  in the negative  $f_z$  direction of twice the radius of the Ewald sphere.

To produce uniform sampling along the  $f_z$ -axis, we need to vary the radius of the Ewald sphere in a linear manner. Consequently, we step the laser frequency  $\nu = c/\lambda$ , which is proportional to the sphere radius, in equal increments rather than step the wavelength  $\lambda$ , which is inversely proportional to the sphere radius. In practice, it is more convenient to monitor the frequency shift  $\Delta\nu$  from the nominal frequency  $\nu_0 = c/\lambda_0$  than it is to monitor the absolute frequency  $\nu = \nu_0 + \Delta\nu$ . Given this preference, the radius of the Ewald sphere of reflection is written as

$$\frac{1}{\lambda} = \frac{1}{\lambda_0} + \frac{\Delta\nu}{c}.$$

Equation 31 can now be recast in the form

$$\Delta\nu = -\frac{c}{2} \left( \Delta f_z + \frac{f_x^2 + f_y^2}{f_{z_0} + \Delta f_z} \right), \quad (34)$$

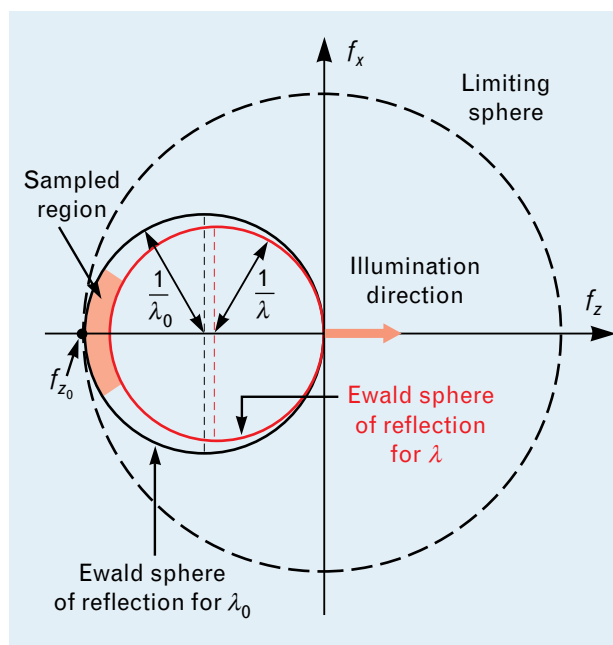


**FIGURE 4.** Ewald-sphere representation for the sampling of the 3D Fourier space of a scattering object. The illumination direction is fixed along the  $f_z$  direction. Constant  $\lambda$  contours lie on the surface of the Ewald sphere of reflection. The radius of the Ewald sphere of reflection is varied by changing the wavelength of the source of illumination. The shaded region represents the sampled region of Fourier space for a near-monostatic measurement configuration.

where

$$\Delta f_z = f_z - f_{z_0} \quad (35)$$

is the spatial-frequency offset from  $f_{z_0}$ . Equation 34 gives the frequency shift  $\Delta\nu$  required for sampling a given point in Fourier space.

Ideally, we would like to sample Fourier space on a rectangular grid to facilitate calculation of the inverse Fourier transform. Although Equation 34 could be used to determine the frequency shift required for individual points on the grid, data acquisition would be tedious and time consuming; Equations 32–34 show that there is a mixing between the effects of the measurement parameters  $x_d$ ,  $y_d$ , and  $\Delta\nu$  on the spatial frequency variables  $f_x$ ,  $f_y$ , and  $f_z$ . Consequently, these parameters would have to be set separately for each point on the grid. For low-resolution to moderate-resolution 3D images, which have range and cross-range resolution lengths that are large com-

pared with the wavelength, the accessible region of Fourier space for a given frequency is approximated by a plane, allowing Equations 32–34 to be linearized as

$$x_d = -\lambda_0 f_x z_d, \quad (36)$$

$$y_d = -\lambda_0 f_y z_d, \quad (37)$$

and

$$\Delta v = -\frac{c}{2} \Delta f_z, \quad (38)$$

respectively. Then the variables are decoupled, and it is possible to sample in parallel by making simultaneous measurements with a fixed detector array and stepping the laser frequency between data frames. Later in this article, in the section on aberrations, we investigate the effects of assuming that Equations 36–38 continue to apply as the resolution of the measurement increases. Techniques for compensating for the resulting aberrations are also described.

### Resolution

We have shown theoretically how 3D images can be formed by measuring the speckle pattern over the surface of a detector array while stepping the laser frequency. The larger the scan length and detector-array size, the larger the volume of Fourier space sampled and the better the achievable resolution. We now write expressions for the resolution-cell size by calculating the width of the 3D point-spread function corresponding to the size of the sampled region of Fourier space.

Let  $F_x$ ,  $F_y$ , and  $F_z$  represent the size of the sampled range of Fourier space in the  $f_x$ ,  $f_y$ , and  $f_z$  directions. These ranges correspond to total detector-array lengths of  $w_x$  and  $w_y$  in the  $x$  and  $y$  directions, and frequency-scan length of  $B$ , respectively. The corresponding resolutions (obtained by Fourier-transforming a 3D rect function having these widths in the three dimensions and selecting values of the arguments of the resulting sinc functions that correspond to the first null) are

$$\Delta x = \frac{1}{F_x} = \frac{\lambda_0 z_d}{w_x}, \quad (39)$$

$$\Delta y = \frac{1}{F_y} = \frac{\lambda_0 z_d}{w_y}, \quad (40)$$

and

$$\Delta z = \frac{1}{F_z} = \frac{c}{2B}. \quad (41)$$

In Equations 39 and 40,  $z_d$  is the distance between the reference point and the observation plane. The resolutions given by Equations 39–41 also correspond to the spacing between planes in image space that result from using the fast Fourier transform (FFT) algorithm to calculate the 3D Fourier transform. Note that Equation 41 is also given as Equation C in the sidebar entitled “Wavelength Dependence of Speckle.” As an example of Equations 39–41, the cross-range resolution is  $\Delta x = \Delta y = 80 \mu\text{m}$  for a detector array of size  $w_x = w_y = 10 \text{ mm}$ , a detector distance  $z_d = 1 \text{ m}$ , and a wavelength  $\lambda_0 = 0.8 \mu\text{m}$ ; the range resolution is  $\Delta z = 30 \mu\text{m}$  for a frequency scan of  $B = 5 \text{ THz}$ . As described in the sidebar on the Ewald sphere, the ultimate resolution, which corresponds to sampling the entire limiting sphere, is  $\Delta x = \Delta y = \Delta z = \lambda/2$ .

For comparison of the transverse resolution given by Equations 39 and 40 with conventional imaging, we rewrite Equation 39 in terms of the half-angle  $\theta_d$  of light received by the detector array as

$$\Delta x = \frac{\lambda_0}{2 \sin \theta_d}. \quad (42)$$

If  $\theta_d$  is interpreted as the cone half-angle of light received by a microscope objective, then Equation 42 is the standard expression relating image resolution to the numerical aperture (equal to  $\sin \theta_d$ ) of a microscope. Thus conventional imaging and speckle-pattern sampling have similar resolution capabilities for general images.

Speckle-pattern sampling, however, actually provides the capability for enhanced resolution of objects consisting of a small number of separated points. For example, the distance between a reference point and an object point can be measured to a resolution better than the grid spacing given by Equations 39–41 by taking advantage of the phase information inherent in the interference pattern. One

approach to extracting this information is to subdivide the voxel representing the image of the point by calculating a discrete Fourier transform (DFT) at points inside this voxel, and to search for the location where the maximum value of the DFT occurs, thus determining the location of the scattering point. A similar procedure can be employed to enhance range resolution for the opaque diffuse scattering objects being considered in this article.

### Aliasing

As described in the sidebar entitled “Wavelength Dependence of Speckle,” the larger the range extent of an object, the smaller the frequency step required to avoid aliasing. Equation D from this sidebar quantifies the maximum frequency-step size allowed for an object of range extent  $L$  (including the reference point) and is repeated here for convenience:

$$\Delta v_{\text{step}} \leq \frac{c}{4L}. \quad (43)$$

Corresponding expressions for the maximum pixel dimensions  $p_x$  and  $p_y$  of the detector array in the  $x$  and  $y$  directions (assuming no decimation of pixels in a frame) are given in terms of the cross-range extents  $D_x$  and  $D_y$  of the object (including the reference point) as

$$p_x \leq \frac{\lambda_0 R_d}{2D_x} \quad (44)$$

and

$$p_y \leq \frac{\lambda_0 R_d}{2D_y}. \quad (45)$$

If the approximate range and cross-range extents of the object are known, then Equations 43–45 can be used to set up the measurement to minimize the number of data points. For example, if the range extent  $L$  of the object is 100 mm (including the reference point), then the laser frequency step size  $\Delta v_{\text{step}}$  must be less than 750 MHz. Likewise, if the cross-range extent of the object is  $\Delta x = \Delta y = 25$  mm (including the reference point), then the pixel size required for a detector distance of  $R_d = 1$  m and a wavelength of  $\lambda_0 = 0.8 \mu\text{m}$  must be  $p_x = p_y \leq 16 \mu\text{m}$ .

### Aberrations

We now summarize the effects, analyzed in Reference 39, of continuing to sample on a rectangular grid in measurement space as resolution increases. We also describe techniques for correcting the resulting aberrations in the 3D image. These aberrations are divided into three types, referred to as wavelength aberration, detector-plane distortion, and depth-of-field aberration.

#### *Wavelength Aberration*

Both wavelength aberration and detector-plane distortion are tied to the  $\lambda R_d$  scaling factor in Equations 32 and 33 that relates position  $(x_d, y_d)$  in the detector plane to spatial frequencies  $(f_x, f_y)$  in Fourier space. Any variation of this scaling factor during the process of sampling Fourier space causes image degradation. Wavelength aberration is image degradation caused by varying  $\lambda$  during a measurement to achieve range resolution. This variation is minimal for the short frequency scans used for low-range-resolution measurements but becomes problematic as the range resolution increases. In terms of the measured speckle pattern, wavelength aberration manifests itself as a wavelength-dependent speckle size. As  $\lambda$  increases, the entire speckle pattern expands about the  $z$ -axis. This expansion causes speckle lobes to shift outward at a rate proportional to the radial distance  $r$  from the  $z$ -axis.

We can gain a better understanding of wavelength aberration by considering its effect on an isolated scattering point located at  $(x_b, y_b, z_b)$ . Consider first the 2D cross-range image formed by Fourier-transforming a single speckle frame. For a speckle frame acquired at the nominal frequency  $\nu_0 = c/\lambda_0$ , the scaling factor that places this image point at the correct position  $(x_b, y_b)$  in the transverse plane is  $\lambda_0 R_d$ . The application of this same scaling factor to frames acquired at a different wavelength  $\lambda$ , however, produces the erroneous position coordinates

$$x'_b = x_b \frac{\lambda_0}{\lambda} = x_b \left( 1 + \frac{\Delta \nu}{\nu_0} \right)$$

and

$$y'_b = y_b \frac{\lambda_0}{\lambda} = y_b \left( 1 + \frac{\Delta v}{v_0} \right).$$

Thus scanning the laser frequency causes the 2D image point to blur out along a radial line in the transverse plane, as illustrated in Figure 5. The total blur length for a frequency scan of bandwidth  $B$  is

$$r_{\text{blur}} = r_b \frac{B}{v_0} = r_b \frac{\lambda_0}{2\Delta z}, \quad (46)$$

where

$$r_b = \sqrt{x_b^2 + y_b^2}$$

is the transverse distance between the scattering point and the reference point.

Equation 46 shows that the size of the blur caused by wavelength aberration is proportional to the transverse distance of the scattering point from the reference point. Therefore, the location of the reference point in the transverse plane plays a role in determining the severity of wavelength-aberration effects, which are reduced if the reference point is near the center of the object. The second form of Equation 46 shows explicitly that the degradation in cross-range resolution caused by wavelength aberration becomes more severe as the range resolution increases. Consequently, we must correct for wavelength aberration to achieve high range resolution and high cross-range resolution simultaneously for an object with large cross-range extent.

We can write a condition for determining when image degradation due to wavelength aberration begins to become significant by deciding on an acceptable blur and solving Equation 46 for  $r_b$ . If we assume that a blur of one-quarter of a transverse resolution cell is acceptable, then the resulting condition is

$$r_b < \frac{\Delta r \Delta z}{2\lambda_0}. \quad (47)$$

In Equation 47,  $\Delta r$  denotes the nominal transverse resolution  $\Delta x$  or  $\Delta y$ . (An alternative derivation of Equation 47 is to calculate the value of  $r_b$  at which the maximum phase error caused by wavelength aberration is equal to  $\pi/2$ .) As an example of the use of

Equation 47, there can be  $r_b/\Delta r = 62.5$  transverse resolution cells between the scattering point and the reference point for a range resolution  $\Delta z$  of 100  $\mu\text{m}$  and a wavelength  $\lambda_0$  of 0.8  $\mu\text{m}$  before wavelength-aberration effects begin to become significant.

There are two general techniques for achieving wavelength-aberration compensation: digital compensation of speckle-size changes, and optical compensation by varying the size of the speckle pattern at the detector plane. The second technique can be implemented by using a lens to adjust the speckle size, or by varying the distance to the detector plane such that  $\lambda R_d$  is fixed. For example, a range resolution  $\Delta z$  of 100  $\mu\text{m}$  at  $\lambda_0 = 0.8 \mu\text{m}$  corresponds to a change in wavelength of 0.4% of the nominal wavelength. Thus wavelength-aberration correction could be accomplished by changing the distance  $R_d$  from the reference point to the detector plane by 0.4% during the frequency scan.

#### *Detector-Plane Distortion*

Detector-plane distortion is also governed by Equations 32 and 33. This aberration corresponds to a

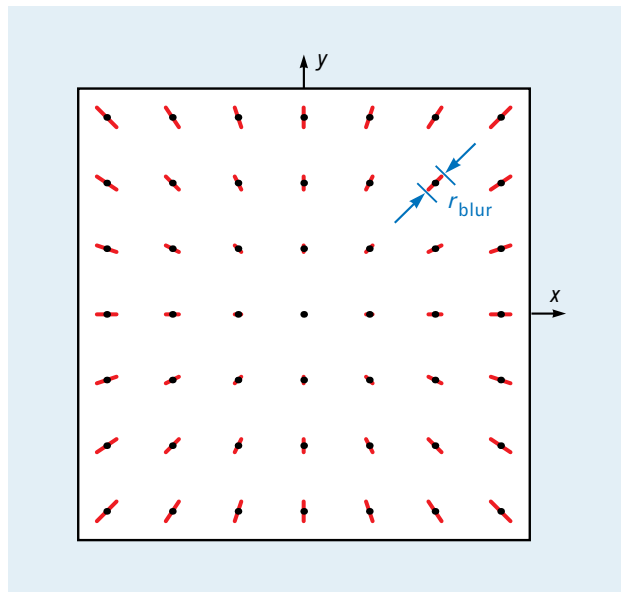


**FIGURE 5.** Radial blurring of image points caused by wavelength aberration. The black points represent the locations of the unaberrated images of a rectangular array of scattering points. The radial blurring due to wavelength aberration, indicated by the red lines, increases with distance from the central reference point.

nonconstant value of  $R_d$ , typically as a result of sampling on a flat detector plane with constant  $z_d$  value, rather than on the interior surface of a sphere of radius  $R_d$ . Another way of describing this difference, illustrated in Figure 6, is that the radial position  $r_d$  of pixels varies as  $\tan \theta_d = r_d/z_d$  for flat detector arrays, rather than as  $\sin \theta_d = r_d/R_d$ , as required by Equations 32 and 33. Detector-plane distortion is insignificant for measurements with low cross-range resolution because the maximum value of  $\theta_d$  is so small that the difference between the value of  $\sin \theta_d$  and  $\tan \theta_d$  is negligible.

The condition for negligible degradation due to detector-plane distortion, obtained by allowing a maximum phase error of  $\pi/2$ , is

$$r_b < \frac{\Delta r^3}{\lambda_0^2} \approx \frac{\lambda_0}{8 \sin^3 \theta_d}. \quad (48)$$

Equation 48 indicates that the effects of detector-plane distortion are more pronounced for object points that are farther away from the reference point and that these effects are very small unless high reso-

lution is required over large fields of view. For example, with  $\lambda_0 = 0.8 \mu\text{m}$  and  $\Delta r = 40 \mu\text{m}$ , a field of view  $r_b$  of 100 mm is achievable without deleterious effects from detector-plane distortion. The corresponding number of resolution cells possible without distortion is given by the ratio  $r_b/\Delta r = 2500$ , which is higher than the number of pixels per side available in typical detector arrays. Consequently, detector-plane distortion does not pose a problem for this situation; it becomes a problem, however, for microscopic applications with high cross-range resolutions. For example, with  $\Delta r = 4 \mu\text{m}$ , the maximum field of view without distortion effects is  $r_b = 100 \mu\text{m}$  so that the ratio  $r_b/\Delta r$  is 25, which severely limits the number of resolution cells in the transverse direction.

Correction of detector-plane distortion can be accomplished digitally, or optically, or through the use of specialized detector arrays. A well-designed 3D imaging system would simultaneously correct for wavelength aberration and detector-plane distortion. In many practical situations, a Fourier-transform lens could be used to simulate far-field detection. This approach provides the opportunity to correct for detec-

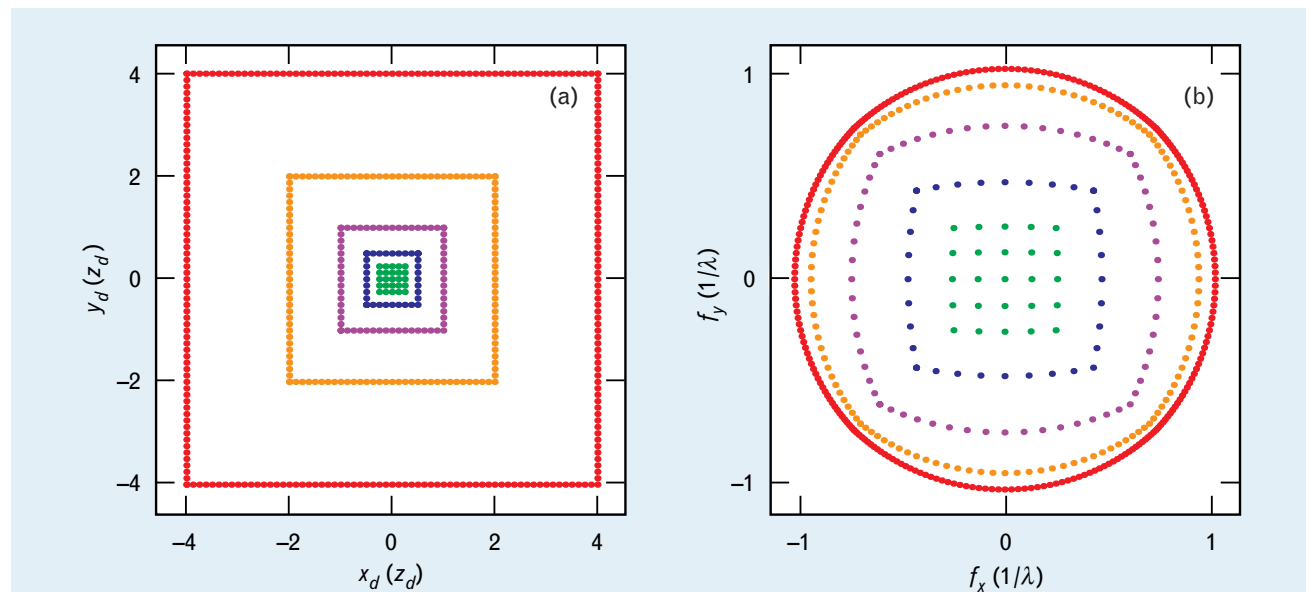


**FIGURE 6.** Detector-plane distortion: (a) pixel locations in the detector plane; (b) mapping to sample-point locations in the  $f_x$ - $f_y$  plane of Fourier space. The green dots correspond to pixels on a square detector grid. The distance  $z_d$  between the detector plane and the laser reference point is twice the width of the detector array. Each successive color represents pixels on the perimeter of a larger detector array. The total width of the array doubles with each successive color. For small values of  $f_x$  and  $f_y$  (represented by the green dots), Fourier space is sampled on an essentially uniform grid, and detector-plane distortion is negligible.

tor-plane distortion in the design of the Fourier-transform lens and to address wavelength aberration. One approach is to design a zoom Fourier-transform lens with variable focal length  $f$  that is varied during the frequency scan such that  $\lambda f$  is constant. Another approach is to design a Fourier-transform lens that is achromatic in the sense that  $\lambda f$  is constant [41, 42].

### *Depth-of-Field Aberration*

Depth-of-field aberration is a result of the fact that the region of Fourier space sampled by a single speckle frame lies on a curved surface—the Ewald sphere of reflection—in Fourier space. For a small enough range of spatial frequencies  $f_x$  and  $f_y$ , the sampled region approximates a plane, and depth-of-field aberration is negligible. The result of depth-of-field aberration is to degrade image points having large range offsets  $z_b$  from the reference point, hence the term depth-of-field aberration.

The maximum range offset that can be achieved without significant degradation from depth-of-field aberration is given by

$$|z_b| < \frac{\Delta r^2}{\lambda_0} \approx \frac{\lambda_0}{4 \sin^2 \theta_d}. \quad (49)$$

Note the similarity between Equation 49 and Equation 48. Because Equation 49 goes as  $\sin^{-2} \theta_d$  rather than  $\sin^{-3} \theta_d$ , depth-of-field aberration is more sensitive to the value of cross-range resolution than is detector-plane distortion.

Equation 49 places stringent requirements on the maximum range extent allowable without degradation. For example, with  $\lambda_0 = 0.8 \mu\text{m}$ , a cross-range resolution of  $\Delta r = 4 \mu\text{m}$  yields a maximum range extent from the reference point of  $|z_b| = 20 \mu\text{m}$ . With  $\Delta r = 40 \mu\text{m}$ , the maximum range extent increases to  $|z_b| = 2 \text{mm}$ . Relaxing the cross-range resolution to  $\Delta r = 400 \mu\text{m}$  achieves a range extent of  $|z_b| = 200 \text{mm}$  without depth-of-field aberration compensation. This depth-of-field behavior is no different from that of conventional imaging, where the lateral resolution determines the depth of field, or from raster scanning with a laser spot, where a tight laser focus at one plane implies a large spread in the spot size at other planes. An advantage of forming 3D images

by speckle-pattern sampling is that this aberration can be corrected in the data processing to yield high-resolution images over large volumes in image space.

To compensate for depth-of-field aberration, we must know the deviation  $\Delta v_{\text{offset}}$  in laser frequency that would be required at each pixel on the detector array to sample 3D Fourier space on a plane rather than on the surface of the Ewald sphere. By inspection of Equation 34, we can write this deviation in terms of the spatial frequencies  $f_x$  and  $f_y$  (corresponding to each pixel) and the spatial-frequency increment  $\Delta f_z$  (defined by Equation 35 and corresponding to a particular speckle frame) as

$$\Delta v_{\text{offset}} = -\frac{c}{2} \left( \frac{f_x^2 + f_y^2}{f_{z_0} + \Delta f_z} \right). \quad (50)$$

Equation 50 provides the key for correcting depth-of-field aberration. The compensation technique is to build up the information required for each flat plane in Fourier space from previous speckle frames, as illustrated in Figure 7. The correct frequency-offset value for each pixel is calculated by Equation 50, from which the corresponding frame-offset number is determined. An interpolation filter is used because previous frames generally do not provide the exact frequency offset that is required for each pixel.

### **Near-Field Effects**

In developing the basic principles of 3D imaging, we have assumed that the observation point  $P_d$  and the source point  $P_s$  are located in the far field of the scattering object. Good images are then obtained as long as any aberrations that may arise from nonuniform sampling of Fourier space can be neglected. An additional source of image degradation is the near-field effects that occur when the observation point or source point is too close to the scattering object for the far-field approximation to hold. Fortunately, however, the dominant aberration that occurs for typical near-field measurements is a distortion of the surface shape rather than a blurring of image points. In this section we summarize results, derived in Reference 39, that can be used to correct this distortion to produce accurate high-quality images well into the near field of the scattering object. An important ben-

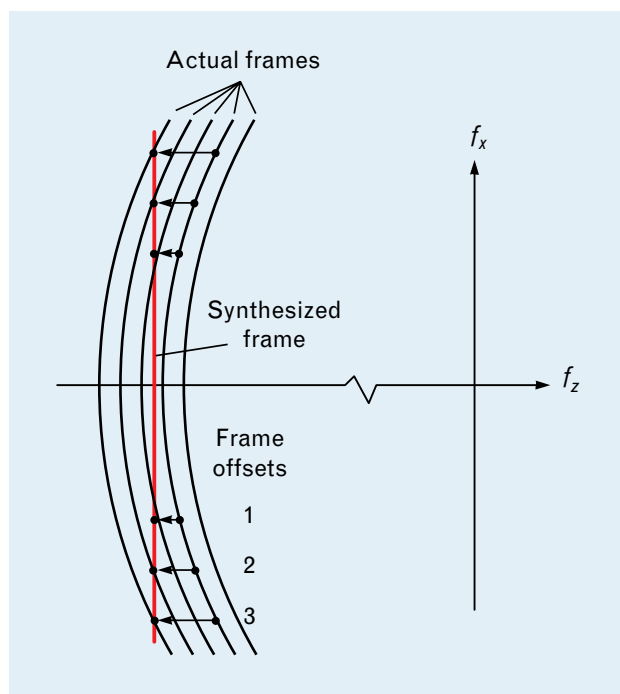


**FIGURE 7.** Technique for correcting depth-of-field aberration. The curved lines represent sampled regions of Fourier space in the  $f_x$ - $f_z$  plane corresponding to successive speckle frames. Compensation is achieved by calculating the frequency offset  $\Delta v_{\text{offset}}$  required by Equation 50 for each  $(f_x, f_y)$  position and each frame and by using previous speckle frames to build up a synthesized speckle frame corresponding to a flat region in Fourier space.

enefit of near-field imaging is that noncollimated illumination and near-field observation can be used for large objects when it is difficult or expensive to simulate far-field conditions by using a large collimating optic.

We begin by listing validity conditions for the results from Reference 39 that follow. First, we assume that Equation 14 for the Fresnel approximation of the distance  $R_{hd}$  and the corresponding condition for  $R_{sh}$ , obtained by substituting the subscript  $s$  for  $d$  in Equation 14, are satisfied. Two additional constraints are

$$z_d > \frac{\lambda_0}{2} \left( \frac{r_b}{\Delta r} \right)^2, \quad (51)$$

and the corresponding condition for  $z_s$  obtained by substituting  $z_s$  for  $z_d$  in Equation 51. The effect of

Equation 51 is to limit the Fresnel approximation to the paraxial region surrounding the  $z$ -axis. This is done by restricting the transverse resolution  $\Delta r$  (and hence the overall size of the detector array) that is allowed for a given transverse object size  $r_b$ . An additional constraint on the detector distance,

$$z_d > \lambda_0 \left( \frac{z_b}{\Delta r} \right)^2, \quad (52)$$

limits the range extent of the object for a given transverse resolution. There is no requirement corresponding to Equation 52 for the position  $z_s$  of the source point, as there is for Equations 14 and 51.

Equation 51 is written in terms of the ratio  $r_b/\Delta r$ , which goes as the number of transverse resolution cells, or pixels, along a line in the image. Consequently, the value of  $r_b/\Delta r$  in Equation 51 does not need to be larger than the number of pixels along an edge of the detector array. For example, even small source-point and observation distances  $z_s$  and  $z_d$  of 100 mm yield an  $r_b/\Delta r$  ratio of 500 for a wavelength  $\lambda_0$  of 0.8  $\mu\text{m}$ . Thus there can be hundreds of transverse resolution cells, and Equation 51 places relatively minor restrictions on practical imaging systems. If the range extent of the object is comparable to its transverse extent, restrictions imposed by Equation 52 will be similar to those from Equation 51.

The main result of the near-field analysis of 3D imaging in Reference 39 is that the dominant near-field effect is image distortion. This distortion is governed by the equation

$$z = h(x - x_{\text{shift}}, y - y_{\text{shift}}) + z_{\text{shift}}, \quad (53)$$

where the shifts in the three coordinates are given by

$$x_{\text{shift}} = x \frac{z - z_{\text{shift}}}{z_d}, \quad (54)$$

$$y_{\text{shift}} = y \frac{z - z_{\text{shift}}}{z_d}, \quad (55)$$

and

$$z_{\text{shift}} = -\frac{x^2 + y^2}{4} \left( \frac{1}{z_s} + \frac{1}{z_d} \right). \quad (56)$$

Because this distortion can be removed computationally, high-quality 3D images can be achieved much farther into the near field than the far-field condition given by Equation 13 would lead us to believe.

Equation 53 is a general result that encompasses both noncollimated illumination (by varying  $z_s$ ) and near-field observation (by varying  $z_d$ ). As  $z_d$  and  $z_s$  approach infinity, Equation 53 reduces to the far-field result given by Equation 25. For far-field observation with noncollimated illumination, Equation 53 takes a particularly simple form:

$$z = h(x, y) + \frac{x^2 + y^2}{4z_s}. \quad (57)$$

Here the error consists simply of an additive curvature term.

The derivation of Equations 53–57 assumes that the distances  $z_s$  and  $z_d$  are held constant during a frequency scan. There is actually an advantage to holding the products  $z_s\lambda$  and  $z_d\lambda$  constant during the measurement. Besides compensating for wavelength aberration, keeping these quantities fixed turns out

to be an optical means for eliminating  $z_{\text{shift}}$  from Equations 54–56. The resulting image then takes the simplified form

$$z = h\left(x - \frac{xz}{z_d}, y - \frac{yz}{z_d}\right). \quad (58)$$

Although nonlinearities in the distortion have been removed, Equation 58 shows that the magnification still varies with range. This remaining distortion can readily be corrected in the data processing to produce accurate high-resolution images in the near field of an object.

### Measurements

We now demonstrate the basic concepts of the speckle-pattern-sampling (SPS) technique. These concepts are demonstrated through laboratory measurements obtained with the optical system depicted in Figure 8. Measurements are then compared with those from a well-known industrial standard. Finally, we present measurement results of an object that required very high range resolution.

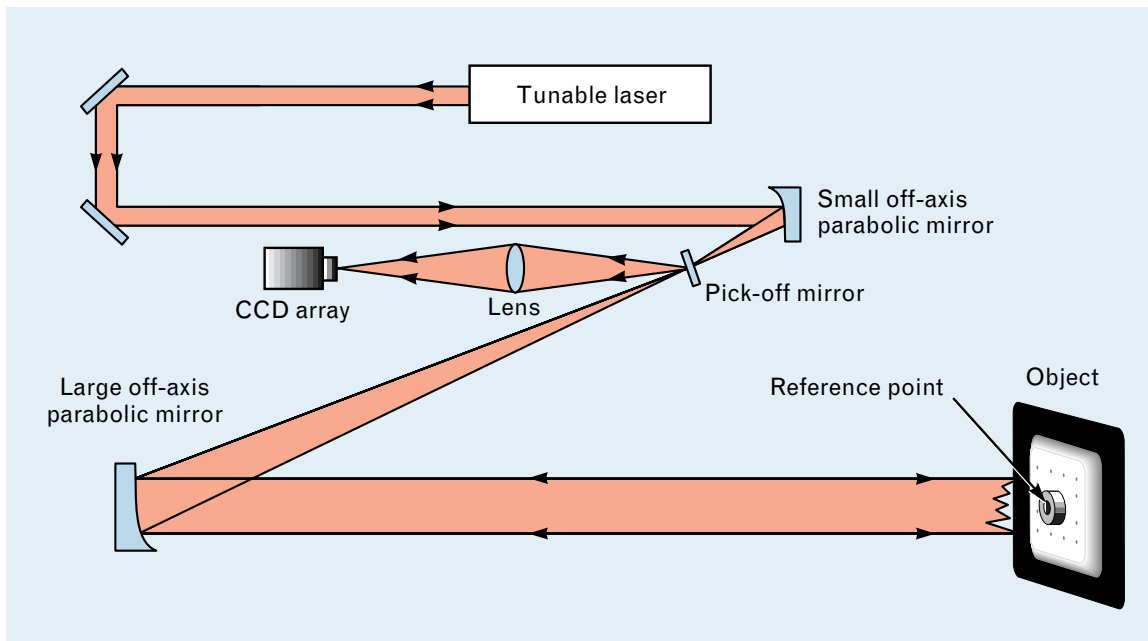


**FIGURE 8.** Schematic diagram of optical system used for speckle-pattern-sampling measurements. The pair of off-axis parabolic mirrors expand the laser beam from the tunable laser and flood-illuminate the object. The pick-off mirror directs the backscattered light into the CCD array in the detector leg. This system satisfies the requirements for far-field illumination and observation.

### *Optical Configuration*

The illumination source for the majority of the measurements presented here was a Coherent, Inc., 899-29 Ti:sapphire ring laser pumped by a Coherent, Inc., Innova 200 argon-ion laser. The Ti:sapphire is an actively stabilized single-frequency ring laser that can produce a coherence length greater than 100 m. This coherence length is more than adequate because it is large compared to the range extent of targets of interest. The laser was typically used at a nominal wavelength of  $\lambda_0 = 0.78 \mu\text{m}$  and tuned over bandwidths of up to 15 THz. Although the Ti:sapphire has a single-frequency output power of greater than 2 W, only a few milliwatts were needed for the measurements presented here.

The optical system in Figure 8 was designed to simulate far-field illumination and observation so that near-field effects are entirely eliminated for objects up to 225 mm in diameter (diameter of large off-axis parabola). The output from the laser is directed to a set of off-axis parabolas that act as a beam-expanding telescope. The beam strikes the small parabola, goes through focus, expands by a factor of twenty-five, and is collimated by the large off-axis parabola. The collimated beam then flood-illuminates the object. The back-scattered light follows the opposite path. It strikes the large parabola, which is now acting as a collector, and is directed to a pick-off mirror located at the focal point of the telescope. Since it is impractical to place a detector at the focal point of the telescope, the pick-off mirror is used to direct the light away from the telescope and onto a CCD array. The array was a  $512 \times 512$ -pixel, 14-bit, scientific-grade research CCD from Photometrics Ltd. A lens is inserted between the pick-off mirror and the CCD array so that the number of pixels per speckle lobe can be adjusted.

### *Demonstration of Concepts*

In this section we demonstrate experimentally that the wavelength-dependent speckle pattern provides range information about the scattering object, and we show that this range information can be combined with the cross-range information available from the spatial dependence of the speckle pattern to

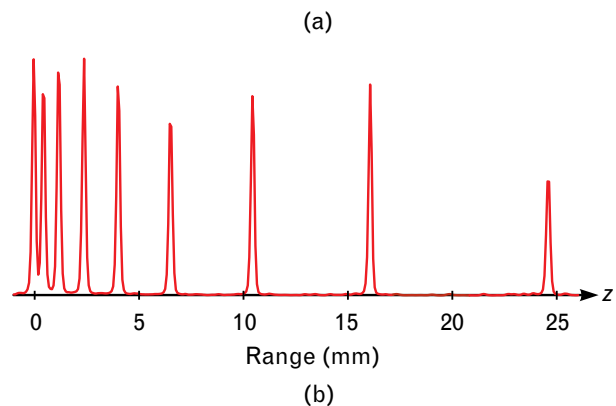
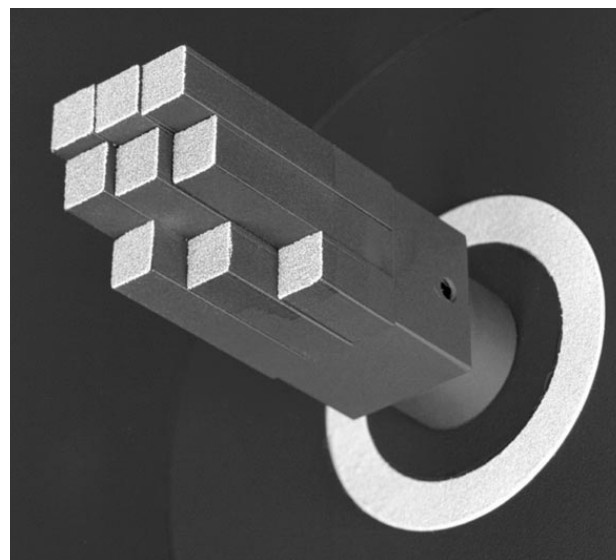


**FIGURE 9.** Laboratory demonstration of submillimeter range resolution from the wavelength dependence of speckle: (a) nine-step range-resolution target mounted in front of a range-reference ring, and (b) range-resolved measurement for a laser-frequency scan length of 2 THz. The smallest step size of 0.5 mm is well resolved in the measurement.

produce high-quality 3D images. We also discuss the measurement parameters that are required to obtain images that are free of aberrations.

Figure 9(a) is a photograph of a target used for demonstrating range-resolved measurements. This target has nine levels with a ratio of 1.4 between successive step heights. The individual step sizes range between 0.5 and 8.5 mm, with a total range span of 24.6 mm. Figure 9(b) shows a range-resolved measurement for a scan length  $B$  of 2 THz, taken from Reference 1. The associated theoretical range resolution given by Equation 41 is 0.075 mm. All nine lev-

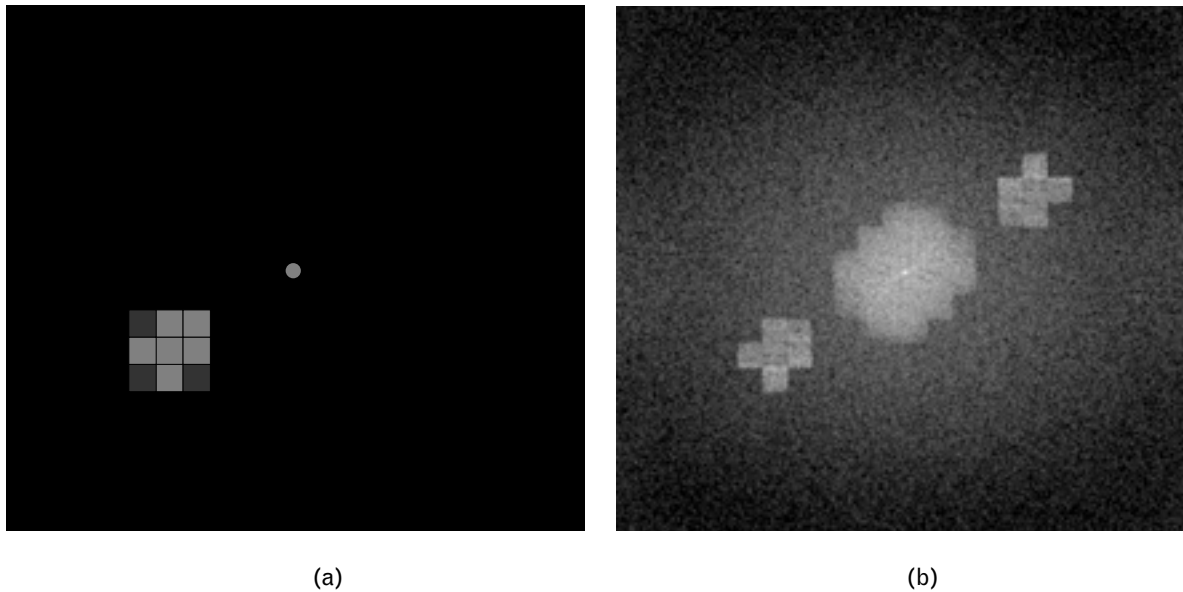


**FIGURE 10.** Cross-range-resolved image of nine-step target with three masked steps: (a) object scene consisting of target and reference point being illuminated into the page, and (b) image obtained from 2D Fourier transform of single speckle frame.

els in the target are accounted for, and even the 0.5-mm step is well resolved, which clearly demonstrates submillimeter range resolution. In this particular measurement, a reference ring was used in place of a reference point.

Figure 10 illustrates that cross-range information can also be obtained from speckle by Fourier-transforming a speckle frame acquired at a single wavelength [43, 44]. The object scene, depicted in Figure 10(a), consists of the nine-step target from Figure 9 and a specular reference point that are illuminated along the axis of the step target. Three of the steps have been masked to make a more interesting object. The reference point is produced by a concave spherical mirror with a 75-mm radius of curvature located 25 mm to the right and 12.5 mm above the top right corner of the target. Figure 10(b) is the magnitude of the Fourier transform of a  $512 \times 512$ -pixel speckle frame from this object scene. The four components of Equation 24 are evident in this figure. Because the reference point is separated from the step target in the transverse direction by more than its cross-range extent of  $D_x = D_y = 19$  mm, the desired image (lower left) is isolated from the autocorrelation function (center) and the polar-symmetric image (upper right).

Let us now consider cross-range resolution. Because of the long focal length ( $f = 2$  m) of the primary mirror, and the small collecting area ( $w_x = w_y = 16$  mm) of the pick-off mirror, the cross-range resolution at  $\lambda_0 = 0.8 \mu\text{m}$  for this optical system is limited to  $\Delta x = \Delta y = 100 \mu\text{m}$  by Equations 39 and 40 (with  $z_d$  replaced by the focal length  $f$  of the collimating optic). The image in Figure 10(b) actually has a transverse resolution of  $\Delta x = \Delta y = 280 \mu\text{m}$ , which corresponds to a speckle magnification by the lens in Figure 8 of  $M = 2.4$  and a detector size of the CCD array of  $w_x = w_y = 13.8$  mm (here  $z_d$  in Equations 39 and 40 is replaced by  $Mf$ ). This transverse resolution also corresponds to 68 pixels along the width of the target.

Now that we have demonstrated how cross-range resolution is obtained from the speckle pattern, we demonstrate 3D imaging by combining range information with cross-range information to produce the full 3D image of the nine-step target shown in Figure 11. For this measurement the 75-mm-radius concave mirror was placed 30 mm behind the bottom step and 10 mm to the side of the target. The desired image component can be isolated in the 3D Fourier transform because the surface of the mirror is offset in range from the target by more than its range ex-

tent. A  $256 \times 256$ -pixel region of the CCD array was selected, and the speckle magnification was set at  $M = 2.5$ , yielding a transverse resolution of  $\Delta x = \Delta y = 575 \mu\text{m}$ . The total frequency span of the measurement was  $B = 320 \text{ GHz}$ , which produced a range resolution of  $\Delta z = 470 \mu\text{m}$ , by Equation 41.

By Equation 43, the maximum frequency-step size allowed for nonaliased imaging of an object with total range extent  $L = 55 \text{ mm}$  (25-mm object depth and 30-mm range offset of reference point) is  $\Delta v_{\text{step}} = 1.4 \text{ GHz}$ . An actual value of  $\Delta v_{\text{step}} = 1.25 \text{ GHz}$  was used in this measurement so that the given scan bandwidth of 320 GHz was achieved with a 256-frame measurement. The height values displayed in Figure 11 were obtained from the magnitude of the 3D Fourier transform by selecting the voxel having the highest value in each column. The step heights in the image agree with the step heights of the target to within the resolution of the measurement.

None of the three aberrations associated with errors in the sampling of Fourier space needs to be corrected in Figure 11. From Equation 47 we find that wavelength aberration is not an issue; the maximum transverse offset of an object point from the reference

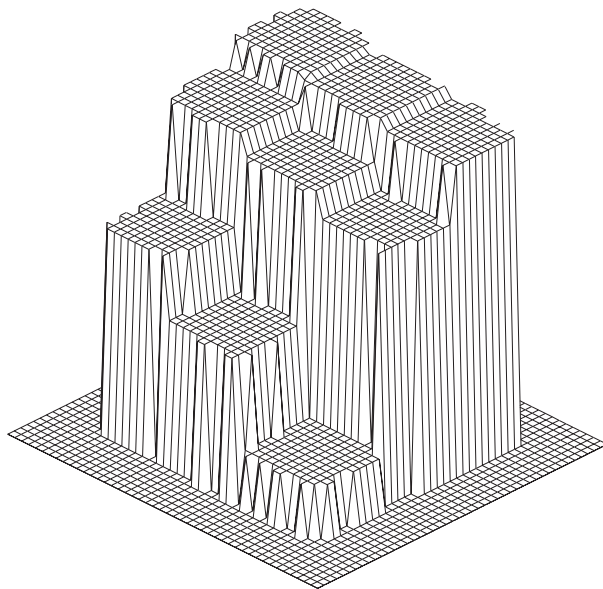


**FIGURE 11.** 3D image of nine-step target obtained by speckle-pattern-sampling technique. Range resolution and cross-range resolution are obtained from the wavelength dependence and the spatial dependence of the speckle pattern, respectively.

point for the given range and cross-range resolutions is  $r_b = 173 \text{ mm}$ , which is larger than the maximum value,  $r_b = 30 \text{ mm}$ , of the object scene. Detector-plane distortion can be entirely ignored for any image made with this optical system because it is negligible by Equation 48 for even the best cross-range resolution and the largest object diameter allowed. By Equation 49, depth-of-field aberration for the transverse resolution of  $\Delta x = \Delta y = 575 \mu\text{m}$  begins to be a problem for points that are offset from the reference point in range by more than  $|z_b| = 400 \text{ mm}$ . This condition is easily satisfied because the range extent of the nine-step target is only 24.6 mm.

If the image in Figure 11 had been formed with the system's maximum transverse resolution of  $\Delta x = \Delta y = 100 \mu\text{m}$ , the maximum allowable range offset from the reference point would have been reduced to  $|z_b| = 12 \text{ mm}$  and the image would have been aberrated. The effect of depth-of-field aberration is to blur the 2D image of each object point by an amount that increases with the range offset  $z_b$  of that object point from the reference point. Thus, without correction of depth-of-field aberration, the only plane in perfect focus is the plane cutting through the reference point. In this regard, depth-of-field aberration is analogous to the limited depth of field encountered in conventional imaging. The higher the resolution, the more rapidly the image degrades in range.

#### *Quantitative Comparison with Industry Standard*

Before the SPS technology can be incorporated into a practical system, we must validate measurement results and compare the system's performance with accepted methods. In this section we compare measurements obtained with the noncontact laser-based SPS technique to those acquired by using a more conventional mechanical method, the coordinate measuring machine (CMM). The CMM is a high-precision contact device that provides measurements of objects in three dimensions and is the industry standard for dimensional metrology. Our intent here is not to demonstrate measurements with the best possible resolutions. Instead, we choose to concentrate on the comparison of the two techniques at some easily achievable resolutions.

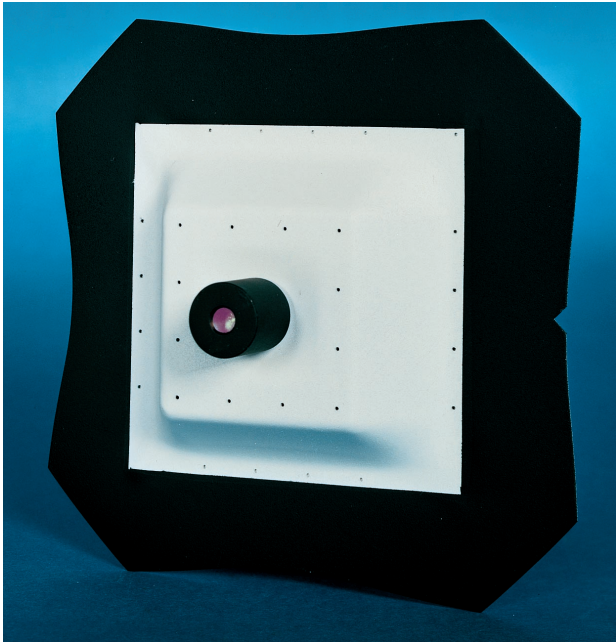


**FIGURE 12.** Stamped sheet-metal test object. The region of interest (painted white) has dimensions of approximately 100 x 100 x 20 mm. A curved reference mirror is mounted in the center of the object.

The object selected for an initial comparison was a steel sheet-metal sample that was stamped with a discrete die at the MIT Laboratory for Manufacturing and Productivity [45]. This object presents a chal-

lenge for most contouring techniques because it contains steep surfaces with slopes ranging between  $45^\circ$  and  $68^\circ$ . Figure 12 shows a photograph of the object. When this object is viewed from the back, it bears a notable resemblance to an ashtray. Consequently, we refer to it as such throughout this section. The region of interest was painted white, and is approximately  $100 \times 100 \times 20$  mm in size. Registration holes with diameters of 1 mm were drilled in the ashtray to aid in the alignment of data sets; the distance between nearest neighboring holes is 15 mm. A 125-mm-focal-length concave mirror is mounted in the center of the object to provide a reference point for the speckle-based measurements.

Contact measurements of the ashtray were conducted by using a Giddings and Lewis RS-50 Apollo II Series Cordax coordinate measurement system. The manufacturer's specifications indicate that this system has a volumetric accuracy of  $10 \mu\text{m}$  and a repeatability of  $2 \mu\text{m}$ . CMM measurements, taken at 1-mm spacings, cover a  $100 \times 100$ -mm grid. The resulting surface contour shown in Figure 13 is quite good; however, we needed approximately ten hours to acquire the 10,000 data points in this measurement. This length of time clearly demonstrates why CMMs are not practical for applications that require high-density surface maps.

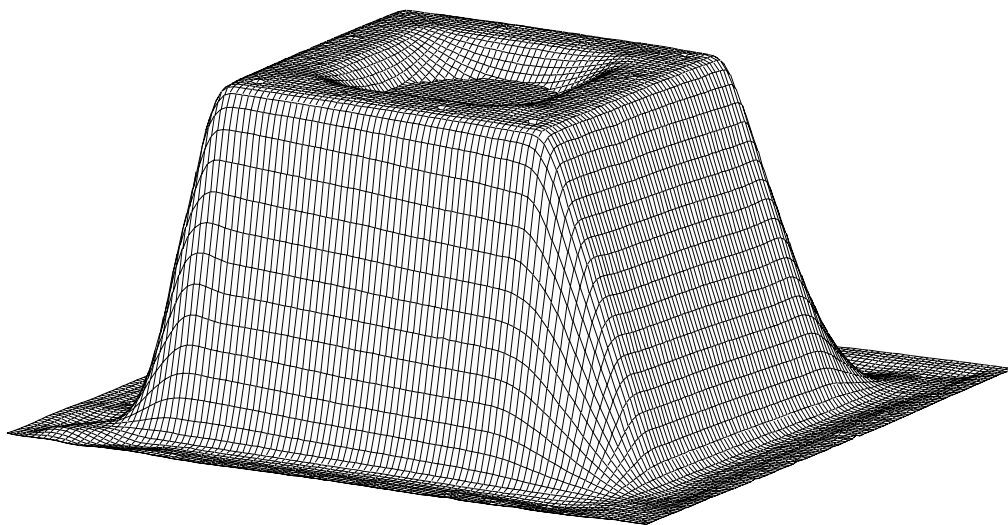


**FIGURE 13.** Coordinate-measuring-machine (CMM) measurement of surface contour of stamped sheet-metal test object. Measurements were taken at a 1-mm spacing and cover a  $100 \times 100$ -mm region of the object.

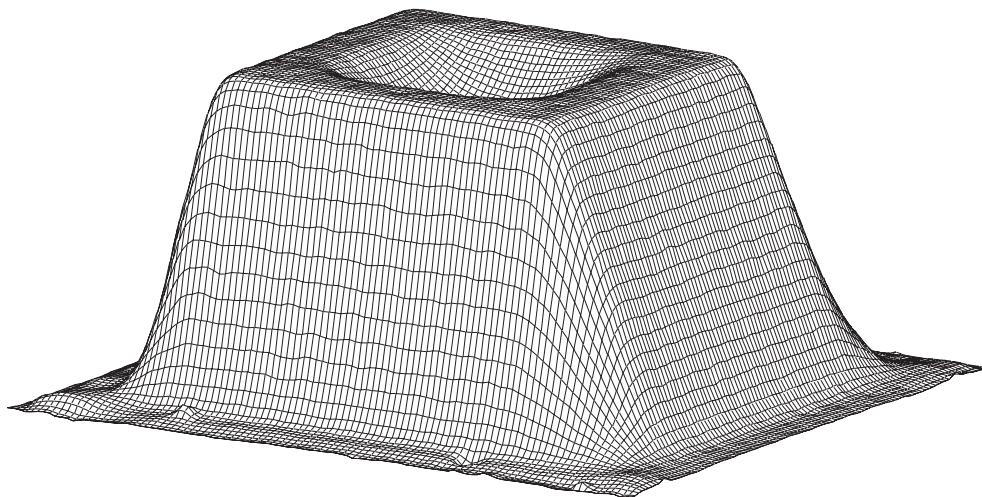


**FIGURE 14.** Speckle-pattern-sampling (SPS) measurement of surface contour of stamped sheet-metal test object. The raw data consisted of two-hundred-fifty-six  $256 \times 256$ -pixel speckle frames with a laser-frequency step of 1.8 GHz between frames.

For the SPS measurements of the ashtray shown in Figure 14, we used reasonably conservative parameters so that aberration compensation was not required. The range extent from the face of the reference mirror to the lowest point on the ashtray is approximately  $L = 40$  mm, which requires a  $\Delta v_{\text{step}}$  of less than 1.88 GHz for nonaliased imaging. An actual frequency-step size of 1.8 GHz was chosen for these measurements. Because of its ease of use and increased tuning rate, we used a Nufocus external-cavity tunable diode laser in lieu of the Ti:sapphire. The Nufocus laser, which has an output power of 5 to 10 mW, was operated at a nominal wavelength of  $\lambda_0 = 0.78 \mu\text{m}$ . A total of 256 images, each  $256 \times 256$  pixels in size, were acquired at 1.8 GHz intervals, yielding a total laser scan length of  $B = 460$  GHz and a range resolution of  $\Delta z = 325 \mu\text{m}$ . For a CCD detector size  $w_x = w_y = 6.9$  mm, a primary-mirror focal length  $f = 2$  m, and a magnification  $M = 2.3$ , a transverse resolution of  $\Delta x = \Delta y = 520 \mu\text{m}$  was obtained.

The time for acquiring the 256 images was approximately thirty minutes. The feedback for this acquisition, however, involved a person verifying that the laser had been tuned to the appropriate wavelength for each frame. Once the wavelength verification is incorporated into the data-acquisition system, acquisition times of well under one minute for a  $256 \times 256 \times 256$  data set should be achievable. The

3D Fourier transforms were computed by using the FFT algorithm on a Sun Microsystems SPARC-20 workstation running Visual Numerics Inc. PV-WAVE software. It took approximately thirty minutes to calculate the  $256 \times 256 \times 256$ -point 3D FFTs with this configuration; a parallel-processing computer could be used to reduce this time to the order of one second.

To compare the measurements shown in Figures 13 and 14, we first had to scale and align the data sets. The CMM data set consisted of  $100 \times 100$  points, while the region of interest in the SPS height function contained  $190 \times 190$  points. The CMM data were interpolated by using standard techniques to obtain a  $190 \times 190$ -point CMM data set. To align the two surfaces, we minimized the distance between corresponding alignment points in each data set by scaling, translating, and rotating the SPS height function. A detailed discussion of the speckle processing and data alignment is given elsewhere [46].

Figure 15(a) is a representative slice through the CMM and SPS surface contours; the two plots are virtually indistinguishable on this scale. Figure 15(b) shows the difference between the two curves. The maximum peak-to-peak difference is on the order of one  $\Delta z$  unit. The curves are in excellent agreement throughout most of the plot, with a slight deviation near the edges. These deviations correspond to areas

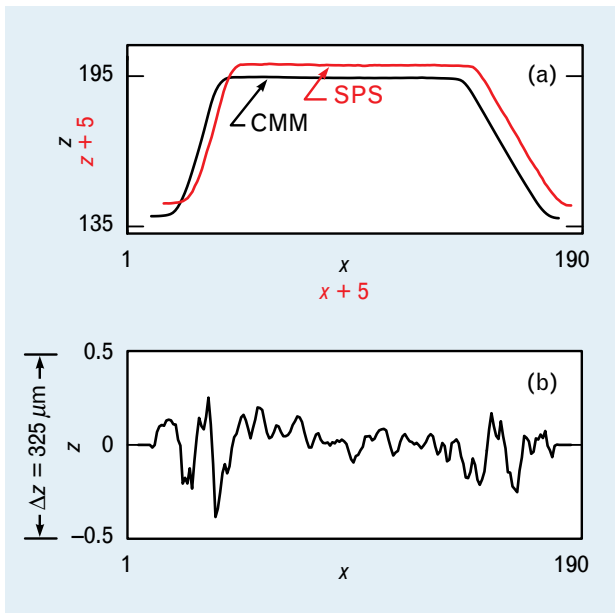


**FIGURE 15.** Comparison of CMM and SPS results for a single slice: (a)  $x$ - $z$  slice through CMM and SPS surface profiles; (b) difference between surface profiles.

of the ashtray that have steeply sloped surfaces. Figure 16(a) shows a difference map of the two surface contours. The central region of this plot, where the reference mirror was mounted, was not included in the statistical calculations. The standard deviation of the differences over the surface is  $\sigma = 0.19 \Delta z$ , which corresponds to approximately  $60 \mu\text{m}$  for this measurement. Again we see that the steeply sloped regions of the ashtray appear to give rise to the greatest difference between the two measurements. Figure 16(b), which is the histogram of the differences between the two contours, shows that the vast majority are within  $\pm 0.5 \Delta z$ . By excluding the steeply sloped regions, we lower the standard deviation of the differences to  $\sigma = 0.13 \Delta z$ , or approximately  $40 \mu\text{m}$ . We recall from Equation 41 that larger frequency-scan lengths result in higher range resolutions. Consequently, if the differences scale in the same manner as the resolutions, we believe that agreement to within a few microns is achievable.

#### *High-Range-Resolution Measurement*

To demonstrate the high range resolutions that are achievable with the SPS technique, we fabricated a second range-resolution target by milling five steps of

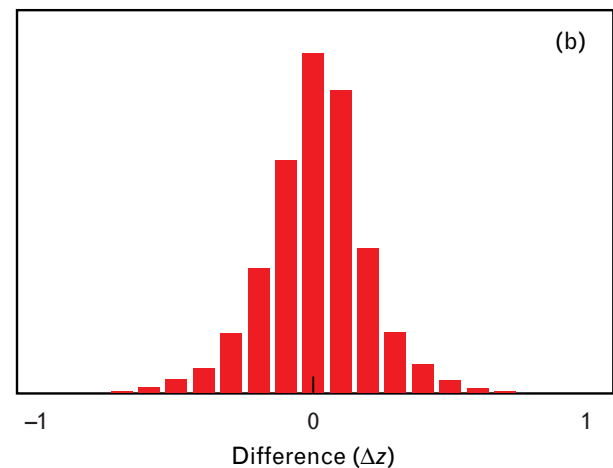
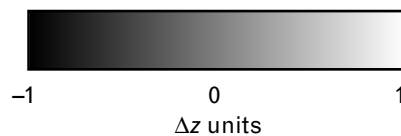
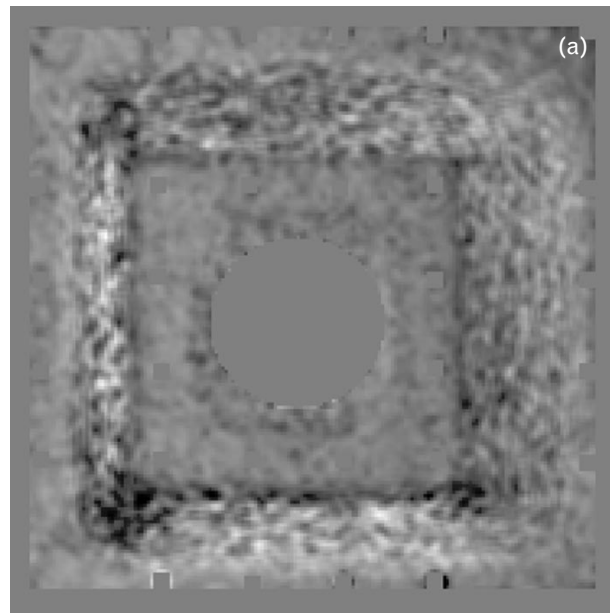


**FIGURE 16.** Comparison of CMM and SPS surface contours: (a) difference map for entire surface; (b) histogram of differences.

various heights in an aluminum plate. The distance between successive levels varies from  $25 \mu\text{m}$  to  $125 \mu\text{m}$  in  $25\text{-}\mu\text{m}$  increments, giving a total target range extent of  $375 \mu\text{m}$ . The transverse dimensions of the individual steps are  $15 \times 50 \text{ mm}$ . Note that even the  $25\text{-}\mu\text{m}$  step is well resolved in range in the 3D image displayed in Figure 17.

The reference point used for this measurement

was a concave 75-mm-radius spherical mirror located 8 mm to the side of the middle step and recessed into the metal so that the surface of the mirror is  $395\ \mu\text{m}$  below the bottom level of the target. The measurement consisted of 256 speckle frames with laser-frequency steps of  $\Delta\nu_{\text{step}} = 60\ \text{GHz}$  between frames, yielding a total frequency span of  $B = 15.3\ \text{THz}$  and a range resolution of  $\Delta z = 9.8\ \mu\text{m}$ . The target was tilted slightly with respect to the illumination beam so that the raw image contained several discrete range steps of value  $\Delta z$  along the length of each step. The DFT technique for subdividing voxels mentioned earlier was applied to enhance range resolution in Figure 17.

The speckle frames used in producing Figure 17 were taken from a  $256 \times 256$ -pixel region of the CCD array and subdivided for averaging into four  $128 \times 128$  subarrays. The height values in Figure 17 are the weighted average from these measurements. The cross-range resolution from the individual arrays is  $\Delta x = \Delta y = 700\ \mu\text{m}$ .

The minimum radius of curvature that yielded a sufficient reference-beam strength relative to the high return from the bare metal steps was 75 mm. The focal point of this mirror occurs at a distance of half of the radius of curvature in front of the mirror and is the position of the reference point when calculating the effects of depth-of-field aberration. Thus the value of  $z_b$  that should be used in Equation 49 for calculating whether depth-of-field aberration is significant is approximately half of this value,  $z_b = 37.5\ \text{mm}$ . Because of the large transverse resolution for this measurement, the allowable range offset  $z_b$  from Equation 49 is many times this value so that depth-of-field aberration can be ignored for this measurement in spite of the relatively large value of  $z_b$ .

Wavelength aberration, on the other hand, is a significant aberration for this measurement; by Equation 47, it degrades the image for object points with transverse offsets from the reference point of only 4 mm. Therefore, wavelength aberration had to be corrected. This correction was accomplished by varying the speckle magnification during the frequency scan through changing the lens and detector spacings in Figure 8 such that  $M\lambda$  remained constant.

Although Figure 17 demonstrates the capability of

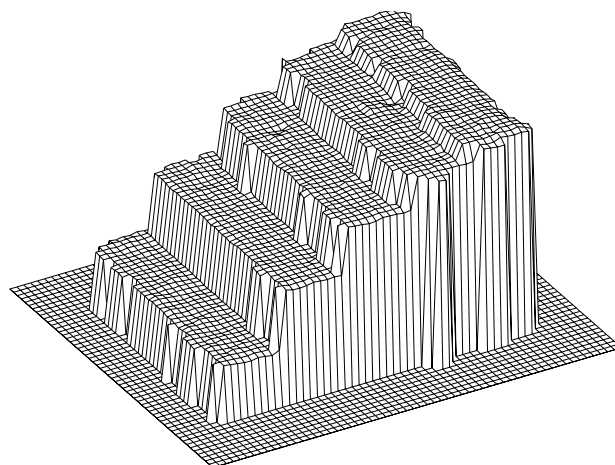


**FIGURE 17.** 3D image of five-step range-resolution target demonstrating a range resolution of better than  $10\ \mu\text{m}$ . The step sizes vary from  $25\ \mu\text{m}$  for the top step to  $125\ \mu\text{m}$  for the bottom step.

the SPS technique to produce images with high range resolutions, the range extent of the test object is rather small. To maintain the same range resolution as the range extent increases requires a smaller laser-frequency step size to avoid aliasing. This, in turn, increases the total number of speckle frames required. The problem is compounded if the same cross-range resolution is maintained as the cross-range extent increases. This increase in the number of cross-range-resolution cells calls for more densely populated detector arrays and increased processing and memory requirements. These factors currently limit the voxel density of the raw 3D image to the order of one thousand cubed.

## Conclusions

In this article we analyze and demonstrate a speckle-pattern-sampling technique for 3D imaging based on the wavelength dependence of laser speckle. Range resolutions of better than  $10\ \mu\text{m}$  were achieved. Surface contours obtained from laboratory measurements were compared with those obtained from an accepted contact method—the coordinate measuring machine. Although speckle-pattern sampling compares well with this industry standard, and we demonstrated a significant speed increase over contact-based techniques, there are still some drawbacks to the technique that limit the variety and number of its

## IMAGE-SPECKLE-BASED 3D IMAGING

THE 3D IMAGING technique described in the main text is based on the wavelength dependence of speckle in the radiation pattern of the scattering object. In this sidebar we describe an alternative 3D-imaging technique based on image speckle—speckle present in the conventional image of a coherently illuminated object. In this alternative technique, we obtain range information from the wavelength dependence of speckle, as before, but we obtain transverse information through conventional imaging. The main advantages of this technique are that the reference beam is supplied automatically and that calculating a 2D Fourier transform of each frame of data is unnecessary. (The imaging property of the lens already produces a one-to-one correspondence between points in the detector array and points in object space.)

Figure A shows the measurement configuration. The beam from a tunable laser is split into two parts and produces two mutually coherent source points  $P_1$  and  $P_2$  separated by the distance  $a$  and located at coordinates  $(x_1, y_1, z_1)$  and  $(-x_1, -y_1, -z_1)$ . The expanding beams from these source points simultaneously flood-illuminate the object, and a lens images the object onto a CCD array. Consider the point  $P$  lying on the surface of the object

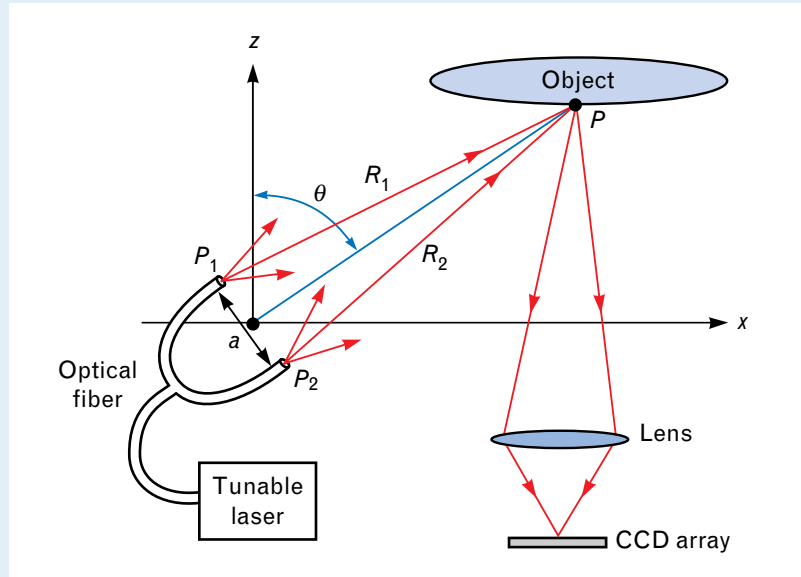


**FIGURE A.** Coordinate system for image-speckle-based 3D imaging.

at position  $(x, y, z)$ . The coordinates  $x$  and  $y$  of this point are known by the location of its image on the detector array. If the  $z$  value corresponding to each value of  $x$  and  $y$  could be determined, then the desired 3D image would be obtained.

We determine the  $z$  value by observing the effect that tuning the laser frequency has on the image speckle. We define  $R_1$  and  $R_2$

to be the distances from the points  $P_1$  and  $P_2$  to the point  $P$ , respectively, and we define  $s$  to be the pathlength difference between these two distances; that is,  $s = R_2 - R_1$ . (Assume the optical path lengths from the split in the optical fiber to the ends of the two fibers are equal.) On average, approximately half of the light reaching a given point on the detector comes from each of the two

**Table A. Determination of  $z$**

$$s = \sqrt{(x + x_1)^2 + (y + y_1)^2 + (z + z_1)^2} - \sqrt{(x - x_1)^2 + (y - y_1)^2 + (z - z_1)^2}$$

$$z = \frac{4(x x_1 + y y_1) z_1 \pm \frac{s}{2} \sqrt{16(x x_1 + y y_1)^2 + (s^2 - 4z_1^2)(s^2 - a^2 - 4x^2 - 4y^2)}}{s^2 - 4z_1^2} \quad (\text{A})$$

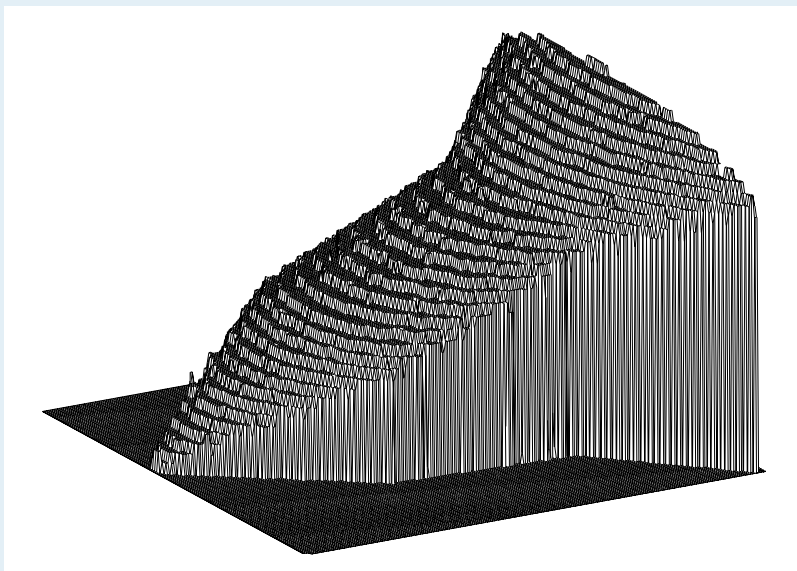


**FIGURE B.** Triconic 3D measurement obtained by using image speckle.

source points. If  $s$  is nonzero, tuning the laser produces relative phase shifts between the contributions from these two points. These phase shifts cause the contributions to alternate between destructive and constructive interference, resulting in a periodic modulation of the speckle intensity. The rate of modulation is proportional to the pathlength difference  $s$ ; the frequency change required to induce one complete oscillation of the speckle intensity is  $c/s$ . Thus  $s$  can be measured at each pixel location by measuring the rate or period of oscillation.

The final step in forming a 3D image is to relate the measured values of  $s$  to the desired quantity  $z$ . This can be done by writing  $s$  in terms of  $z$  and the known quantities  $(x, y)$  and  $(x_1, y_1, z_1)$  and then solving for  $z$ , as shown in Table A. All quantities on the right side of Equation A are

known so that  $z$  is determined for each pixel in the conventional image. For the situation indicated by Figure A, the negative sign in the numerator is the correct choice of signs.

The ratio of the resolution  $\Delta s$  of the pathlength-difference measurement to the range resolution  $\Delta z$  in the 3D image is given by the partial derivative of  $s$  with respect to  $z$ :

$$\frac{\Delta s}{\Delta z} = \left| \frac{\partial s}{\partial z} \right|. \quad (\text{B})$$

The magnitude of this ratio varies between 0 and 2 and generally increases as the bistatic angle  $\theta$  in Figure A approaches  $90^\circ$ . The optimal value of 2 is normally unachievable in practice. A typical value of the ratio for measurement parameters suggested by Figure A is  $|\partial s / \partial z| = 0.2$ .

To estimate range resolution with Equation B, we must first

determine  $\Delta s$ . For a frequency scan of length  $B$ , the resolution in  $s$  obtained by counting whole intensity oscillations is  $c/B$ . Therefore, the resolution in  $s$  for a fractional resolution  $\Delta N$  in the number of cycles  $N$  is

$$\Delta s = \frac{c}{B} \Delta N. \quad (\text{C})$$

For a frequency scan of  $B = 15$  THz and for  $\Delta N = 1$  (counting only whole-number cycles), Equation C predicts that  $\Delta s = 20 \mu\text{m}$ . Substituting this value into Equation B and using  $|\partial s / \partial z| = 0.2$  yields a range resolution of  $\Delta z = 100 \mu\text{m}$ .

Figure B is a 3D image of a 50-mm-long triconic obtained by using the image-speckle technique. The discrete range steps correspond to counting whole number cycles ( $\Delta N = 1$ ). The resolution can be improved by various techniques for reducing  $\Delta N$ , for example, by using a discrete Fourier transform to subdivide cycles.

The image-speckle technique is well suited to the measurement of large contoured parts such as airframe and autobody panels. Here the whole surface can be illuminated from a fairly low angle, providing good range resolution. Drawbacks of the technique are that the depth of field of the 3D image is limited to the depth of field of a conventional imaging system and that certain regions of an object may be shadowed because the angle  $\theta$  between illumination and observation directions is nonzero.

practical applications. One drawback is that it requires a reference point to be located in the vicinity of the object being imaged. We have developed, however, a wavelength-dependent-speckle technique that does not require a reference point (see the sidebar entitled "Image-Speckle-Based 3D Imaging"). In addition, obtaining 3D images from the 3D autocorrelation function of an object, which also does not require a reference point, is an active area of research [39, 48–50]. Another drawback is the high cost of components such as tunable lasers and parallel-processing computers, which makes a system based on speckle-pattern sampling uneconomical at this time.

Many methods for 3D imaging described in the literature have been incorporated into practical systems [47]. In general, these methods are based on one or more of the following principles: physical contact, time of flight, carrier modulation, interference, or triangulation. The speckle-pattern-sampling technique has several advantages over techniques based on these principles. It is noncontact based and can rapidly image an entire object without the need for raster scanning; it can measure complex and irregular shapes having discontinuities and steep-sloped surfaces; it does not require a bistatic angle between the source and detector, thereby eliminating shadowing; and its range resolution does not degrade with distance from the object, making it attractive for applications involving long-range imaging.

### Acknowledgments

This work was supported under the auspices of the Lincoln Laboratory Advanced Concepts Program and the U.S. Army Space and Strategic Defense Command. The authors acknowledge the contributions and support of Marc D. Bernstein, Charles F. Bruce, Vincent W.S. Chan, Thierry B. Copie, Kent R. Edwards, John M. Fini, David E. Hardt, William E. Keicher, Wade M. Kornegay, Herbert Kottler, Charles K. Meins, Jr., Michael S. Mermelstein, Harold Z. Ollin, Harold C. Payson, Charles M. Rader, Patrick K. Rennich, Kenneth R. Roth, Carl S. Singelais, David H. Staelin, John A. Tabaczynski, Mark L. Tincknell, and John R. Vivilecchia.

## REFERENCES

1. L.G. Shirley, E.D. Ariel, G.R. Hallerman, H.C. Payson, and J.R. Vivilecchia, "Advanced Techniques for Target Discrimination Using Laser Speckle," *Linc. Lab. J.* 5 (3), 1992, pp. 367–440.
2. P.P. Ewald, "Theory of X-Ray Interference," *Phys. Zs.* 14 (11), 1913, pp. 465–472.
3. R.W. James, *The Optical Principles of the Diffraction of X-Rays* (Bell, London, 1958).
4. R. Hosemann and S.N. Bagchi, *Direct Analysis of Diffraction by Matter* (North-Holland, Amsterdam, 1962).
5. M. Nieto-Vesperinas, *Scattering and Diffraction in Physical Optics* (Wiley, New York, 1991).
6. E. Wolf, "Three-Dimensional Structure Determination of Semi-Transparent Objects from Holographic Data," *Opt. Commun.* 1 (4), 1969, pp. 153–156.
7. E. Wolf and R.P. Porter, "On the Physical Contents of Some Integral Equations for Inverse Scattering from Inhomogeneous Objects," *Radio Sci.* 21 (4), 1986, pp. 627–634.
8. N.N. Bojarski, "The Far Field in Terms of the Spatial Fourier Transform of the Sources and Its Implications on the Inverse Problem," *J. Appl. Phys.* 58 (1), 1995, pp. 1–5.
9. T.-H. Chu, "Optimal Methodologies in Inverse Scattering Utilizing Wavelength, Polarization and Angular Diversity," Ph.D. thesis, University of Pennsylvania, Philadelphia (1983).
10. H.P. Baltes, ed., *Inverse Scattering Problems in Optics* (Springer-Verlag, Berlin, 1980).
11. P.C. Sabatier, ed., *Basic Methods of Tomography and Inverse Problems* (Adam Hilger, Bristol, U.K., 1987).
12. N. George and A. Jain, "Space and Wavelength Dependence of Speckle Intensity," *Appl. Phys.* 4 (3), 1974, pp. 201–212.
13. N. George, A. Jain, and R.D.S. Melville, Jr., "Experiments on the Space and Wavelength Dependence of Speckle," *Appl. Phys.* 7 (3), 1975, pp. 157–169.
14. N. George, "The Wavelength Sensitivity of Back-Scattering," *Opt. Commun.* 16 (3), 1976, pp. 328–333.
15. N. George, "Speckle from Rough, Moving Objects," *J. Opt. Soc. Am.* 66 (11), 1976, pp. 1182–1194.
16. N. George, A.C. Livanos, J.A. Roth, and C.H. Papas, "Remote Sensing of Large Roughened Spheres," *Opt. Acta* 23 (5), 1976, pp. 367–387.
17. N. George, "Speckle," *SPIE* 243, 1980, pp. 124–140.
18. N.H. Farhat, "Holography, Wave-Length Diversity and Inverse Scattering," in *Optics in Four Dimensions-1980*, M.A. Machado and L.M. Narducci, eds. (American Institute of Physics, New York, 1981), pp. 627–642.
19. C.K. Chan and N.H. Farhat, "Frequency Swept Tomographic Imaging of Three-Dimensional Perfectly Conducting Objects," *IEEE Trans. Antennas Propag.* 29 (2), 1981, pp. 312–319.
20. J.Y. Wang, "Imaging Laser Radar—An Overview," *Proc. 9th Int. Conf. Lasers '86, Orlando, Fla., 3–7 Nov. 1986*, pp. 19–29.
21. J.L. Meyzonnnette and G. Saccomani, "Imaging CO<sub>2</sub> Laser Radar—A Comparison of Three Techniques: LFM Pulse Compression, FMCW, CW," *SPIE* 999, 1988, pp. 91–99.
22. E.M. Strzelecki, D.A. Cohen, and L.A. Coldren, "Investigation of Tunable Single Frequency Diode Lasers for Sensor Applications," *J. Lightwave Technol.* 6 (10), 1998, pp. 1610–1618.
23. L.J. Sullivan, B.E. Edwards, and W.E. Keicher, "The Firepond High Power Carbon Dioxide Laser Radar System," *Proc. Int.*

- Conf. Radar '89 2, Paris, 24–28 Apr. 1989*, pp. 353–357.
24. L.G. Shirley, "Speckle Decorrelation Techniques for Remote Sensing of Rough Objects," *OSA Annual Mtg. Tech. Dig. 18* (Optical Society of America, Washington, 1989), p. 208.
  25. L.G. Shirley, "Speckle Decorrelation," *Proc. IRIS Targets, Backgrounds, and Discrimination 1, Monterey, Calif., 23–25 Jan. 1990*, pp. 123–145.
  26. A.L. Kachelmyer, "Range-Doppler Imaging with a Laser Radar," *Linc. Lab J. 3* (1), 1990, pp. 87–118.
  27. D. Klick, "A Laser Radar Experiment in Space: Firepond Images the Firefly Rocket," *Proc. Int. Conf. on Lasers '90, San Diego, 10–14 Dec. 1990*, pp. 289–300.
  28. D.J. McClure, "Diode Laser Radar: Applications and Technology," *SPIE 1219*, 1990, pp. 446–456.
  29. D.J. Schertler and N. George, "Comparison of Wavelength Scanning and Pulse Echo Systems in Remote Sensing," *Opt. Commun. 77* (1), 1990, pp. 91–98.
  30. L.G. Shirley, "Remote Sensing of Object Shape Using a Wavelength Scanning Laser Radar," *OSA Annual Mtg. Tech. Dig. 17* (Optical Society of America, Washington, 1991), p. 154.
  31. L.G. Shirley and J.R. Vivilecchia, "Target Characterization Using a Wavelength Scanning Laser Radar," *Proc. Second Annual Automatic Target Recognizer Systems and Technology Conf., Fort Belvoir, Va., 17–18 Mar. 1992*, pp. 33–60.
  32. W. Krohn and W. Matthews, "Multispectral Diode-Based Imaging Laser Radar," *SPIE 1633*, 1992, pp. 294–303.
  33. J.C. Marron and K.S. Schroeder, "Three-Dimensional Lensless Imaging Using Laser Frequency Diversity," *Appl. Opt. 31* (2), 1992, pp. 55–262.
  34. J.C. Marron and T.J. Schulz, "Three-Dimensional, Fine-Resolution Imaging Using Laser Frequency Diversity," *Opt. Lett. 17* (4), 1992, pp. 285–287.
  35. T. Dresel, G. Häusler, and H. Venzke, "Three-Dimensional Sensing of Rough Surfaces by Coherence Radar," *Appl. Opt. 31* (7), 1992, pp. 919–925.
  36. K.I. Schultz, S.A. Davidson, A.J. Stein, and J.K. Parker, "Range Doppler Laser Radar for Midcourse Discrimination: The Firefly Experiments," *2nd Annual AIAA SDIO Interceptor Technology Conf., Albuquerque, N.Mex., 6–9 June 1993*.
  37. L.G. Shirley and P.A. Lo, "Bispectral Analysis of the Wavelength Dependence of Speckle: Remote Sensing of Object Shape," *Opt. Soc. Am. A 11* (3), 1994, pp. 1025–1046.
  38. M. Takeda and H. Yamamoto, "Fourier-Transform Speckle Profilometry: Three-Dimensional Shape Measurements of Diffuse Objects with Large Height Steps and/or Spatially Isolated Surfaces," *Appl. Opt. 33* (34), 1994, pp. 7829–7837.
  39. L.G. Shirley and G.R. Hallerman, "Applications of Tunable Lasers to Laser Radar and 3D Imaging," *Technical Report 1025*, MIT Lincoln Laboratory, DTIC #AD-A306557 (26 Feb. 1996).
  40. C.E. Halford, W.L. Gamble, and N. George, "Experimental Investigation of the Longitudinal Characteristics of Laser Speckle," *Opt. Eng. 26* (12), 1987, pp. 1263–1264.
  41. C. Brophy, "Design of an All-Glass Achromatic-Fourier-Transform Lens," *Opt. Commun. 47* (6), 1983, pp. 364–368.
  42. G.M. Morris and D.A. Zweig, "White-Light Fourier Transformations," in *Optical Signal Processing*, J.L. Horner, ed. (Academic, San Diego, 1987).
  43. P.S. Idell, J.R. Fienup, and R.S. Goodman, "Image Synthesis from Nonimaged Laser-Speckle Patterns," *Opt. Lett. 12* (11), 1987, pp. 858–860.
  44. D.G. Voelz, J.D. Gonglewski, and P.S. Idell, "Image Synthesis from Nonimaged Laser-Speckle Patterns: Comparison of Theory, Computer Simulation, and Laboratory Results," *Appl. Opt. 30* (23), 1991, pp. 3333–3344.
  45. D.F. Walczyk, "Rapid Fabrication Methods for Sheet Metal Forming Dies," Ph.D. thesis, Dept. of Mechanical Engineering, MIT, Cambridge, Mass. (1996).
  46. G.R. Hallerman and L.G. Shirley, "A Comparison of Surface Contour Measurements Based on Speckle Pattern Sampling and Coordinate Measuring Machines," *SPIE 2909*, 1996, pp. 89–97.
  47. J.L.C. Sanz, ed., *Advances in Machine Vision* (Springer-Verlag, New York, 1989).
  48. J.R. Fienup, T.R. Crimmins, and W. Holsztynski, "Reconstruction of the Support of an Object from the Support of Its Autocorrelation," *J. Opt. Soc. Am. 72* (5), 1982, pp. 610–624.
  49. R.G. Paxman, J.H. Seldin, J.R. Fienup, and J.C. Marron, "Use of an Opacity Constraint in Three-Dimensional Imaging," *SPIE 2241*, 1994, pp. 116–126.
  50. J.M. Fini, "Three Dimensional Image Reconstruction from Fourier Magnitude Measurements," B.S./M.S. thesis, Dept. of Electrical Engineering and Computer Science, MIT, Cambridge, Mass. (1997).



**LYLE G. SHIRLEY** is a staff member in the Signature Studies and Analysis group of the Radar Measurements division. His primary research interests are in wave phenomenon, random processes, signal processing, and machine vision. He received a B.S. degree and an M.S. degree, both in physics, from Brigham Young University. After receiving a Ph.D. in optics from the University of Rochester in 1988, he joined Lincoln Laboratory, where he began an investigation of the information that laser speckle carries about the scattering object. Currently he is leading an effort to develop prototype 3D imaging systems for solving industrial problems in manufacturing and inspection.



**GREGORY R. HALLERMAN** is an assistant staff member in the Signature Studies and Analysis group of the Radar Measurements division. His current research interests are in high-speed noncontact 3D imaging, image processing, and reflectance spectroscopy. He received a B.S. degree in optics from the University of Rochester and an M.S. degree in electrical engineering from Tufts University. Prior to joining Lincoln Laboratory in 1990, he worked for the University of Rochester's Laboratory for Laser Energetics, where he helped develop liquid crystal polarizer/isolators and liquid crystal waveplates. In his spare time, Greg competes in track and field, where he has won New York state championships in the decathlon and pentathlon.